Synthesis and Evaluation of Super Resolution Compatible Gephyrin Probes

Synthese und Evaluation von Gephyrinsonden für hochauflösende Mikroskopieverfahren

Doctoral thesis for a dental doctoral degree
at the Graduate School of Life Sciences,
Julius-Maximilians-Universität Würzburg,
Section Biomedicine

submitted by

Noah Frieder Nordblom
from

Germersheim

Würzburg 2022

Submitted on: ……..……..

Office stamp

Members of the Thesis Committee:

Chairperson: Prof. Dr. Klaus Brehm

Primary Supervisor: Dr. Hans Michael Maric

Supervisor (Second): Prof. Dr. Camen Villmann

Supervisor (Third): Prof. Dr. Gernot Stuhler

Date of Public Defence: ……..……

Date of Receipt of Certificates: …….

Contents

Summary

This decade saw the development of new high-end light microscopy approaches. These technologies are increasingly used to expand our understanding of cellular function and the molecular mechanisms of life and disease. The precision of state-of-the-art super resolution microscopy is limited by the properties of the applied fluorescent label. Here I describe the synthesis and evaluation of new functional fluorescent probes that specifically stain gephyrin, universal marker of the neuronal inhibitory post-synapse. Selected probe precursor peptides were synthesised using solid phase peptide synthesis and conjugated with selected super resolution capable fluorescent dyes. Identity and purity were defined using chromatography and mass spectrometric methods. To probe the target specificity of the resulting probe variants in cellular context, a high-throughput assay was established. The established semi-automated and parallel workflow was used for the evaluation of three selected probes by defining their co-localization with the expressed fluorescent target protein. My work provided $NN1D_c$ and established the probe as a visualisation tool for essentially background-free visualisation of the synaptic marker protein gephyrin in a cellular context. Furthermore, $NN1D_A$ became part of a toolbox for studying the inhibitory synapse ultrastructure and brain connectivity and turned out useful for the development of a label-free, high-throughput protein interaction quantification assay.

Zusammenfassung

Neuentwickelte, hochauflösende Fluoreszenzmikroskopieverfahren sind prinzipiell geeignet, molekulare Mechanismen und zelluläre Vorgänge im niedrigen Nanometerbereich aufzulösen. Die maximal erreichbare Auflösung wird unter anderem von der eingesetzten Fluoreszenzmarkierung beeinflusst. In dieser Arbeit beschreibe ich die Synthese neuartiger, funktioneller, fluoreszierender Proben und evaluiere deren Eigenschaft Gephyrin, einen universalen Marker der neuronalen inhibitorischen Postsynapse, zu visualisieren. Hierzu wurden Peptide mittels Festphasenpeptidsyntese hergestellt und mit fluoreszierenden Farbstoffen konjugiert, die für hochauflösende Mikroskopieverfahren geeignet sind. Der Syntheseerfolg und die Reinheit der Stoffe wurde mittels massenspektrometrischer und chromatographischer Methoden bestimmt. In einem Hochdurchsatzverfahren wurden die Proben in einem zellulären Kontext untersucht, spezifisch Gephyrin zu markieren. In einem semi-automatisierten, parallelen Verfahren wurden drei ausgewählte Proben synthetisiert und deren Kolokalisation mit dem fluoreszierenden Zielprotein in transfizierten HEK-Zellen untersucht. Aus dieser Arbeit ist $NN1D_C$ hervorgegangen, eine peptidische Sonde zur Visualisierung von Gephyrin. Diese Probe weist verbesserte Färbeeigenschaften wie eine höhere Spezifität und Sensitivität, verglichen mit bisher bekannten peptidischen Gephyrinsonden, auf. Darüber hinaus kann $NN1D_A$ als hochaffiner Binder von Gephyrin zur Entwicklung neuer gephyrinbindender Moleküle in einem high-througput Verfahren genutzt werden.

Abbreviations

BSA. bovine serum albumine
DCM. dicloromethane
DIEA. N-ethyl-N-(propan-2-yl)propan-2-amine
DMEM. dulbecco's modfied eagle medium
DMF. dimethylformamide
DMSO. dimethyl sulfoxide
DNA. deoxyribonucleic acid
FA. formic acid
FBS. fetal bovine serum
Fmoc. fluorenylmethyloxycarbonyl
FP. fluorescent protein
GABA. γ-aminobutyric acid
$GABA_AR$. $GABA_A$ receptor
gephE. gephyrin E-domain
GephHEK. eGFP-gephyrin expressing HEK293T
GFP. green fluorescent protein
GlyR. glycine receptor
HEK293T cells. human embryonic kidney 293 cells
HPLC. reverse phase high performance liquid chromatography
LCMS. liquid chromatography-mass spectrometry
LSCM. laser scanning confocal fluorescence microscopy
MeCN. acetonitrile
MeOH. methanol
MST. microscale thermophoresis
NHS. N-hydroxysuccinimide
nM. nanomolar
oxyma. ethyl cyanohydroxyiminoacetate
PBS. phosphate buffered saline
peg. polyethylene glycol
PEI. polyethylenimine
PFA. paraformaldehyde
Pip. piperidine
POI. protein of interest
PPI. protein-protein interaction
PSD. postsynaptic density
PSF. point spead function
ROI. region of interest
rpm. revolutions per minute
RT. room temperature
sCy5. sulfoCyanine5
SNR. signal-to-noise ratio
SPPS. solid-phase peptide synthesis
STED. stimulated emission depletion
STORM. stochastic optical reconstruction microscopy
TFA. trifluoroacetic acid
TRIC. temperature related intensity change
Vol. volume
WT. wild type

1 Introduction

1.1 Fluorescence Microscopy

Recent advancements in fluorescence microscopy push the boundaries of optical microscopy beyond the resolution limit formulated by Ernst Abbe in 1873. Some of those efforts namely stimulated emission depletion (STED) and stochastic optical reconstruction microscopy (STORM) were awarded the Nobel prize in chemistry 2014. During the Nobel prize announcement speech, chairman Professor Sven Lidin mentioned [1]:

"We see new things, but we see that there are more things to see."

Making use of the advancements in fluorescence microscopy and in order to "*see more things"*, there is a need for labels and probes with new characteristics, suitable for super resolution microscopy. Among those characteristics, label size and compatibility of the fluorescent dye with STORM for example are of great importance.

1.1.1 Diffraction Limited Imaging

After Ernst Abbe, the resolution *d* in nm of an image can be calculated by:

Equation 1 Optical resolution *d*

$$d = \frac{\lambda}{2\,NA}$$

where λ [nm] is the wavelength of light and NA is defined as the numerical aperture [dimensionless quantity] specific to an objective [2]. In other words, the special resolution of an imaging system can be defined by the smallest distance between two points that can be resolved with a specific objective. Due to the diffraction and interference of light that is transmitted through a circular aperture, the resulting signal at the focus is not a single spot but a three-dimensional diffraction pattern, also referred to as airy disk or point spread function (PSF) with a main peak and multiple orders of diffraction. These two PSFs are considered as resolved if their maxima are separated by the full width half maximum (FWHM) as shown in Figure 1 [2].

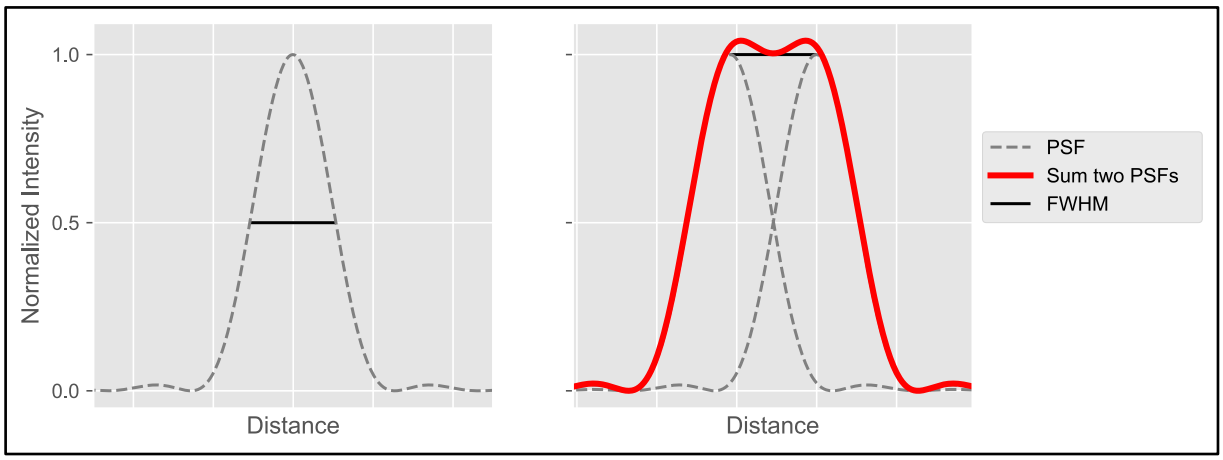

Figure 1 Resolution of an object is limited by the width of the point spread function. On the left, a single two-dimensional representation of a PSF with a main peak and its first order of diffraction is depicted. The full width half maximum is indicated as a black line. On the right-hand side, the overlap of two PSFs in red is separated by the full width half maximum (FWHM).

An example for diffraction limited imaging is confocal microscopy. Contrary to wide-field illumination techniques, where the whole specimen is illuminated and imaged at the same time, confocal microscopy allows for separation of out-of-focus light from the image. This is achieved by a pinhole aperture placed in front of the detector, which allows only light from a diffraction-limited focal volume to pass. The size of the pinhole can be manually adjusted and is reduced for higher resolution or increased for greater sensitivity. Laser-scanning confocal microscopy is a variation of confocal microscopy that allows for selective illumination of the sample, thus reducing photobleaching [3].

1.1.2 Super-resolution Imaging

Super-resolution microscopy approaches collect more data on the specimen that is imaged. These optical data can be of different origins. Their origin can either be of

- deterministic techniques
- stochastic single-molecule localisation techniques

1.2 Deterministic Techniques

Structured illumination microscopy (SIM) and stimulated emission depletion (STED) are examples of deterministic, sub-diffraction-limit imaging techniques. These techniques make use of the fact, that only defined fluorophores are excited via a defined illumination of the specimen known as Moiré pattern (SIM) or that their emission is partially depleted by an additional light source (STED). For STED a resolution of up to 16 nm in X-direction has been reported (*see* Table 1) [3].

1.2.1 Stochastic Single-molecule Localisation Microscopy Techniques

Among other stochastic single-molecule localisation microscopy techniques, stochastic optical reconstruction microscopy (STORM) makes use of the properties of distinct fluorescent dyes that they can switch between their fluorescent on-state and their nonfluorescent off-state under certain conditions at a given time-point. By observing multiple, individual blinking events of distinct fluorophores, multiple fluorophores that are specially located within the diffraction limit of light can be stochastically discriminated [4].

Table 1 Resolution for distinct microscopy methods. Adapted from Heintzmann and Ficz 2013 and modified [5].

Method	**Common abbreviation**	**Best resolution [nm]**
Widefield	WF	230 (XY), 1000 (Z)
Confocal	CLSM	180 (XY), 500 (Z)
Single-molecule localisation	PALM, STORM	20 (XY)
Structured illumination	SIM	100 (XY)
Stimulated emission depletion	STED	18 (X), 20 (XY), 50 (Z)

1.3 Labelling Techniques

A fluorescent dye can either be integrated in a protein of interest (POI) using fluorescent protein fusion techniques or incorporated in fluorescent affinity probes directed against an epitope present in the POI.

1.3.1 Fluorescent Protein Fusion

In 2008, the Nobel prize in chemistry was dedicated to the discovery and subsequent developments of the green fluorescent protein (GFP) for its use as a fluorescent protein tag [6]. Thus, DNA constructs of a POI and a fluorescent protein (FP) can be designed an incorporated into cells via vectors. This leads to the expression of FP-protein constructs which can be visualised and tracked in living and fixed cells by fluorescence microscopy. Today, a cornucopia of different FP constructs with distinct fluorescent properties is available [7]. However, experiments with FP expressing cells must be carefully planned and evaluated as their expression can alter cell physiology and protein function [8, 9].

Another tool was introduced with the development of genetic code expansion, where unnatural amino acids can be incorporated into proteins which can be conjugated to fluorescent dyes [10, 11]. Additionally, these approaches ignore the complex physiological gene regulation that results in the presence of protein isoforms. These protein isoforms can greatly vary across developmental stages as well as tissues, cell-types and even at the subcellular level.

1.3.2 Fluorescent Affinity Probes

Fluorescent affinity probes can be envisioned as three partite complexes:

- targeting moiety
- linker
- fluorescent dye

Labelling efficiency of the protein of interest depends on affinity of the probes in a cellular context. It is heavily influenced by the thermodynamic binding affinity, which can be described as free energy that is released when the binding surfaces of the probe and the protein of interest engage with each other, and water molecules are released from these surfaces. This energy encompasses non-covalent intermolecular interactions including electrostatic interactions, hydrogen bonding, hydrophobic forces and van der Waals forces between POI, probe and solvent as well as changes in degrees of freedom of these molecules.

Affinity can be expressed in form of the equilibrium dissociation constant K_D with the molar concentration of the protein-ligand complex (LP) relative to the molar concentrations of protein (P) and ligand (L). k_{on} $\left[\frac{1}{M \cdot s}\right]$ specifies the on-rate, whereas k_{off} $\left[\frac{1}{s}\right]$specifies the off-rate.

$$\mathrm{L+P} \underset{k_{\mathrm{on}}}{\overset{k_{\mathrm{off}}}{\leftrightharpoons}} \mathrm{LP}$$

Equilibrium K_D is reached when $k_{on} = k_{off}$, which can be written as:

Equation 2 Dissociation constant K_D

$$K_D = \frac{\mathrm{L+P}}{\mathrm{LP}} = \frac{k_{\mathrm{off}}}{k_{\mathrm{on}}}$$

For the development of a highly sensitive and selective probe, a highly affine targeting moiety is beneficial in order to increase specificity by reducing unspecific binding to other parts of the probe [12].

Two important metrics in the context of affinity probes include sensitivity and specificity. A high sensitivity is reached if all POIs (true positive) are stained by the affinity probe.

Equation 3 Sensitivity

$$\text{sensitivity} = \frac{\text{positive}}{\text{true positive}}$$

A high specificity is reached, if the affinity probe does not stain (negative) other proteins (true negative) except the POI.

Equation 4 Specificity

$$\text{specificity} = \frac{\text{negative}}{\text{true negative}}$$

1.4 Affinity Determination

Microscale thermophoresis (MST) is a tool for quantifying protein-protein interactions with little sample consumption. These methods exploit that thermophoresis, the phenomena that molecules move in solutions within temperature gradients, is highly sensitive towards changes of physicochemical parameters (temperature related intensity change (TRIC) among others) and hence useful for discriminating bound from unbound proteins. MST allows to accurately define protein binding affinity in solution . F_{norm} (normalised intensity [‰]) is measured as the ratio of the fluorescence readout before (F_0) and after (F_1) an infrared-laser induced temperature change [13, 14].

Equation 5 Normalised intensity F_{norm}

$$F_{norm} = \frac{F_1}{F_0}$$

Peptide microarrays on the other hand side can also be used to characterise binding between POI and bound peptide ligands. They allow for a very high throughput, but analysis must be performed carefully, and binding is characterised in a semi-quantitative rather than in a quantitative manner. The readout in peptide microarrays is a non-dimensional intensity value at a specific location of the array. Arrays are usually not imaged at thermodynamic equilibrium, thus the predominant effect investigated is k_{off}, which correlates well with the actual binding affinity [15, 16].

1.5 Avidity

Avidity is the sum of affinities of individual binding events, also referred to as functional affinity. A simple and well described example of avidity in protein-protein interactions are IgD, IgE or IgG type antibodies, which harbour two antigen binding sites in a single molecule. Vauquelin and Charlton explained enhanced affinities of these antibodies to their antigens with an increased probability of the second binding evet due to an increased local concentration [17]. This effect could also be shown for nanobodies, which consist of a variable domain of an antibody (V_H), where dimerization of two nanobodies directed against overlapping epitopes on the chemokine receptor CXCR4 increased affinity 27-fold [17].

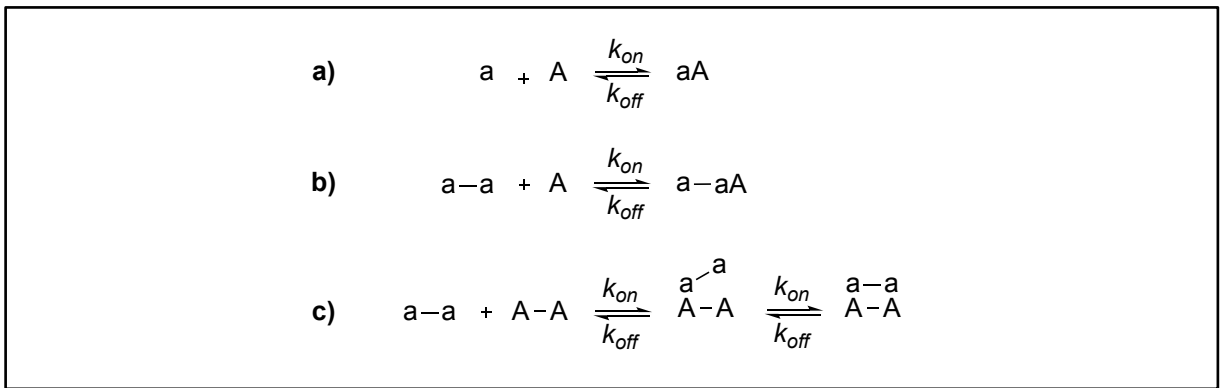

Figure 2 Schematic representation of ligand receptor binding modes for monovalent and multivalent probes. **a)** shows a binding event of a monovalent probe (a) binding to a monovalent receptor (A). **b)** shows a multivalent probe (a-a) binding to a monovalent receptor (A). Due to the simulated concentration increase (a-a) of the binding site (A), k_{on} is increased. **c)** shows a multivalent probe (a-a) targeting a multivalent receptor. Either monovalent or bivalent binding can occur. Once, the probe is bivalently bound to receptor (A–A) and one binding site detaches, rebinding is likely due to proximity.

1.6 Commonly Used Affinity Probes

The first fluorescently labelled antibodies were reported by Coons et al. in 1942 [18]. Since then, protocols have been optimised and antibody labelling is used extensively in immunofluorescence. This is because antibodies can be produced via established protocols for many protein targets [19]. For conventional confocal fluorescence microscopy with a XY-resolution of 180 nm and a Z-resolution of 500 nm, fluorescently labelled antibodies with a size of 10 nm as well as primary and secondary antibody complexes with a size of 20 nm pose a suitable tool for labelling POIs [20, 21]. With the increase in resolution of modern super-resolution microscopy techniques described earlier with a lateral resolution of up to 16 nm, antibody labelling would account for a major linkage error with the same dimension as the resolution itself [22]. An overview of affinity probes with size relations is given in
Figure 3.

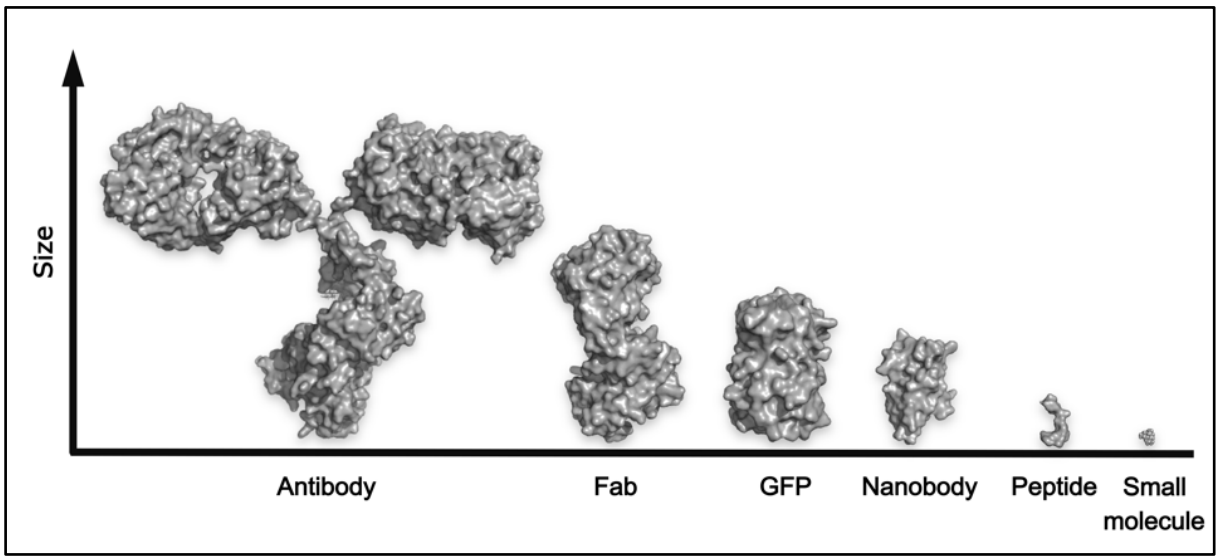

Figure 3 Relative size of distinct fluorescent tags and affinity probes. PDB entries: Antibody: 1IGT, Fragment antigen-binding 4QXG, GFP: 3OGO, Nanobody: 3OGO, Peptide: provided by Maric (RVZ Würzburg), Small Molecule: 6FGD. Relative sizes are approximations.

Not only is the fluorescent dye displaced from the epitope (Table 2, Condition 1), but it was also shown that for tiny structures such as microtubules, the labelling pattern produced by antibody labelling has shown significant wider gaps between labelled epitopes (Table 2, Condition 2) compared to smaller biomolecules such as nanobodies [23]. This fact is most likely caused by steric hinderance by the relatively large antibody complex [20]. This is one of the factors why nanobodies have widely gained attention in the field of super-resolution microscopy [24]. Recent efforts to develop nanobodies directed against synapse components demonstrated the difficulty to label gephyrin specifically in neurons and brain slices [25].

Table 2 Microscopy benefits from small linkage error and high labelling density. Schematic representation of targets (grey) and labels (red). Condition 3 symbolises a smaller linkage error compared to Condition 1 and a higher labelling density compared to Condition 2.

Condition	Target and Label	Label alone
1	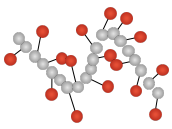	
2		
3		

1.7 Peptide Probes

In the field of molecular imaging, peptide probes offer a lower immunogenicity and a faster biodistribution when compared to antibodies [26]. The first peptide probe (DTPAoctreotide) was approved in 1994 by the United States Food and Drug Administration (FDA) [27]. It was functionalised with the radio nucleotide ^{111}In and used in scintigraphy to visualise distinct somatostatin receptors in the diagnosis of endocrine tumours [28]. Meanwhile, peptides functionalised with fluorophores enter the field of molecular imaging. Although their use is preclinical, they offer a great potential for improving intraoperative detection of distinct cell types like cancer cells, peripheral neurons or bacteria and fungus [26].

In the field of fluorescent microscopy however, only a few peptide probes have been published so far. Among other peptide probes published, SiR-actin, a cyclo-depsipeptide jaspakinolide conjugated to a silicon-rhodamine derivative, binding to the highly abundant, cytoskeletal protein F-actin was published in 2014 by Lukinavičius et al. This compound allows for STED or SIM microscopy in live cells [29].

In 2016, Maric et al. could show that known protein-protein interactions (PPIs) can be used as a starting point for the development of fluorescent peptide probes. The developed probes may be first examples of a new class of superior super-resolution compatible functional labels that can be obtained by exploiting known PPIs [30].

1.8 Inhibitory Synapses

Synapses allow for transmission and modulation of signal between two neurons. The transmission can either be through direct contact of two neighbouring neurons via gap junctions or chemical. A chemical synapse is formed by both a pre- and postsynaptic membrane separated by about 20 nm from each other (synaptic cleft). Transmitters are released into the synaptic cleft upon excitation of the presynaptic neuron at the presynaptic membrane. For inhibitory synapses, neurotransmitters such as γ-aminobutyric acid (GABA) and Glycine bind ligand-gated ion channels at the postsynaptic membrane such as the $GABA_A$ receptor ($GABA_AR$) and glycine receptor (GlyR) [31]. $GABA_A$ receptors allow for the influx of Cl^- ions, causing hyperpolarization within the postsynaptic neuron. This reduces subsequentially the probability of an action potential being fired [31]. The process of chemical information transmission at a chemical synapse is highly modifiable but still regulated in order to allow proper function while maintaining flexibility, also referred to as synaptic plasticity [32].

1.9 Synaptic Plasticity

Synaptic plasticity is necessary in order to allow for strengthening or weakening of a synapse over time. The inhibitory postsynaptic plasticity for example is strongly dependent on the inhibitory postsynaptic density (iPSD), a complex molecular assembly [32]. Among other functions, the iPSD is greatly involved in the clustering of inhibitory receptors at the postsynaptic membrane. A cornucopia of scaffolding and adapter proteins, signalling molecules and cytoskeletal elements take part in this dense, highly flexible and versatile complex [32].

1.10 Gephyrin

The gephyrin protein acts a scaffolding protein of the iPSD in mammals. It consists of the N-terminal G- and C-terminal E-domain, which could be resolved via X-ray crystallography (Protein Data Bank entries 1IHC and 2FU3 [33, 34]). In these crystal structures, the E-domain forms homodimers whereas the G-domain forms homotrimers. The central region between these domains, however, is intrinsically unstructured and displays extensive post translational modifications at multiple sites [35]. The gephyrin E-domain harbours a universal receptor binding site that controls the mutually exclusive recruitment of GlyR and $GABA_ARs$ [36]. Gephyrin acts as a central interaction site for inhibitory neurotransmitter receptors, and proximity ligation mass spectrometric approaches revealed that gephyrin is in close spatial proximity to all major proteins and protein complexes mediating fast synaptic inhibition [37]. The molecular mechanisms that would allow a single scaffold protein to act as scaffold within a highly diverse and large pool of inhibitory synapses is currently unknown. One hypothesis is that an extended array of gephyrin isoforms, generated by alternative splicing, generates diversity at the inhibitory synapses [38]. At least 9 of the 29 exons of the GPHN gene were shown to be subject to alternative splicing in species-, tissue-, cell- and/or environmentally specific manners [38].

We choose gephyrin as a protein target for the following reasons:

- Gephyrin acts as a hallmark for the inhibitory synapse [39], thus reports a structure of major relevance to brain function and specifically represents the proteome of a distinct class of inhibitory post-synapses [37].
- The numbers of gephyrin molecules have been quantified [40] and gephyrin numbers were early recognized to be interdependent with receptor numbers [39]. Thus, the quantity visualisation of gephyrin allows to directly estimate synaptic strength. Synaptic

plasticity mechanisms and improved tools to study synapse plasticity are of immediate and broad interest to the neurobiology field.

- The iPSD and specifically Gephyrin are thought to organise in nanoscale with an estimated thickness of 20 nm [32]. The resolution gain using our compact labels may therefore allow to discover new structures and study modes of plasticity that could not be resolved using conventional immunogenic labels.
- Dozens, more likely hundreds of Gephyrin isoforms are expressed with distinct cell and tissue specificity which most likely bear distinct clustering and localisation properties. The currently used conventional immunogenic labelling strategies visualise only the fraction of isoforms that harbour the relevant epitope. The probes presented in this work act as functional labels. Thus, visualising gephyrin isoforms with the capacity to act as neurotransmitter-receptor scaffold.
- The probes presented in this work harbour great potential for live imaging applications and CLEM. These methods do not allow for conventional gephyrin labelling because of the incompatibility with sample preparations (CLEM) or poor membrane penetration (live imaging).

1.11 Solid-phase Peptide Synthesis

Solid-phase peptide synthesis (SPPS) was first described by Bruce Merrifield in 1963. This technique is a simple, efficient and repetitive peptide synthesis strategy suitable for automation. It makes use of a non-soluble resin that serves as the core of the growing peptide chain. Thus, reagents and solvents used can be removed rapidly and efficiently. Commercially available resins for SPPS are available with different linkers, that allow for the attachment of the first amino acid). In the applied Fmoc strategy contrary to the ribosomal peptide synthesis, SPPS of a desired peptide is performed from the C-terminus to the N-terminus [41]. The amino acids used are orthogonally protected at their Nα-amino group and their reactive side chain for directed peptide growth. The protection group at the Nα-amino group is removed after coupling using steric hindered bases such as piperidine. In the following step, an activated building block is introduced to elongate the growing peptide chain. Due to the orthogonality of the protection groups used, the side chain stays protected until the peptide reaches the desired length. The protection groups from the side chains are removed simultaneously to cleavage of the peptide from the resin [42].

A main advantage of the Fmoc strategy is its safety and efficiency and thus compatibility with automated synthesis robots and a wide variety of commercially available building blocks. For example, site specific post translational modifications like phosphorylated, glycosylated amino

acid building blocks or linkers are commercially available and can be introduced during automated peptide synthesis [42].

2 Materials

2.1 Equipment

Equipment that was used in this thesis is listed in Table 3.

Table 3 List of equipment used.

Device	Source	Product name
Autoclave	Systec	V-150
Balances	Mettler Toledo	XS105
	A&D Company ldt.	FZ-300i
Centrifuges	VWR	Mega Star 1.6R
Dewar	Thermo Scientific	Nalgene 4150-4000 Dewar Flask
Dish washer	Miele	G 7883 CD
Ice machine	ZIEGRA Eismaschinen	094775
Lyophilizer	UNIEQUIP	UNICRYO MC-2L-60°C
Lyophilizer pump	UNIEQUIP	UNIVAC D08RC.8D
Magnetic stirrer	Heidolph	MR 3002
		MR Hei-Mix L
Microscope	Leica	TCS SP5
Peptide synthesizer	Intavis	MultiPep RSi
pH-meter	VWR	pH 1100 L
Pipette	Rainin	Pipet-Lite LTS Pipette L-1000XLS+
		Pipet-Lite LTS Pipette L-200XLS+
		Pipet-Lite LTS Pipette L-20XLS+
		Pipet-Lite LTS Pipette L-2XLS+
Precision cuvette	Hellma	104-10-40
Pump	KNF	N86 LABOPORT
Shaker/incubator	Eppendorf	Thermo Mixer C
Spectrophotometer	Jenway	7205
	Horiba	FluoroMax 4
	PeqLab	NanoDrop ND1000
Thermometer	IKA	ETS-D5
Vortex	Scientific Industries	Vortex-Genie 2
Water purification system	Thermo Scientific	Barnstead GenPure xCAD Plus

2.2 Chemicals and Antibodies

All chemicals were purchased from Carl Roth, Iris, Sigma-Aldrich or VWR. Table 4 specifies chemicals that were used in cell assays.

Table 4 List of chemicals and antibodies used in assays.

Name	Source	Identifier	Lot
Antibodies			
Mouse monoclonal anti-gephyrin, purified IgG, K.O.,3B11	Synaptic Systems	147111	
Alexa Fluor™ 555 goat anti-mouse IgG (H+L)	Life Technologie Corporation		2090527

Mounting Media			
Mowiol	AG Heinze	N.A.	N.A.
	Roth	0713.1	349278961
Chemicals			
Methanol for HPLC	Sigma	34860-2.5L-M	STBH5930
Ammonium chloride	Sigma	A9434-1KG	BCBX4165
Glycine	Roth	3187.3	478277568
Glyoxal solution	Sigma	128465-100G	STBH7639
Natrium chloride	Roth	0962.1	419289120
Paraformaldehyde	Roth	0335.2	458277367
Poly-D-lysine	Corning		
Sucrose	Sigma	S0389-500G	SLCB1570
Triton X-100	Roth	3051.3	298273714
Proteins			
Bovine Serum Albumin	Roth	3737.3	309286793/ 518278803
Peptides			
$_c$VK14	Vladimir Khayenko, AG Maric, RVZ Würzburg		

2.3 Amino Acids and Derivatives for SPPS

All amino acids and derivatives used in SPPS and listed in Table 5 were protected at their N-terminus (Fmoc) and if applicable at the respective side chain with orthogonal protection groups.

Table 5 List of amino acids and derivatives used in SPPS.

Derivative	Code	Chemical name (abbr.)	Source	Identifier
peg-linker	peg	Fmoc-O2Oc-OH	Iris	FAA1435
L-Alanine	A	Fmoc-L-Ala-OH ·H_2O	Iris	FSP1005
L-Cysteine	C	Fmoc-L-Cys(Trt)-OH	Iris	FSC1040
L-Aspartic acid	D	Fmoc-L-Asp(tBu)-OH	Iris	FSP1020
L-Glutamic acid	E	Fmoc-L-Glu(tBu)·H_2O	Iris	FSP1045
Glycine	G	Fmoc-Gly-OH	Iris	FSA1175
Glycine	G*	Boc-Gly-OH	Novabiochem	8.53000.0100
L-Histidine	H	Fmoc-L-His(Trt)-OH	Iris	FSP1090
L-Isoleucine	I	Fmoc-L-Ile-OH	Iris	FSC1110
L-Lysine	K	Fmoc-L-Lys(Boc)-OH	Iris	FSC1125
L-Lysine*	K*	Fmoc-L-Lys(Fmoc)-OH	Iris	FAA1435.0005
L-Leucine	L	Fmoc-L-Leu-OH	Iris	FSP1120
L-Methionine	M	Fmoc-L-Met-OH	Iris	FAA1150
L-Asparagine	N	Fmoc-L-Asn(Trt)-OH	Iris	FSC1015
L-Proline	P	Fmoc-L-Pro-OH·H_2O	Iris	FAA1185
L-Glutamine	Q	Fmoc-L-Gln(Trt)-OH	Iris	FSC1043
L-Arginine	R	Fmoc-L-Arg(Pbf)-OH	Iris	FSC1010
L-Serine	S	Fmoc-L-Ser(tBu)-OH	Iris	FSC1190
L-Threonine	T	Fmoc-L-Thr(tBu)-OH	Iris	FSP1210

L-Valine	V	Fmoc-L-Val-OH	Iris	FSC1245
L-Tryptophan	W	Fmoc-L-Trp-(Boc)	Carl Roth	9668
L-Tyrosine	Y	Fmoc-L-Tyr(tBu)-OH	Iris	FSP1230

2.4 Consumables

Consumables are specified in Table 6.

Table 6 List of consumables.

Consumable	Source	Specification
Gloves	SHIELD Scientific	SHIELDskin ORANGE NITRILE 300
	STARLAB	StarGuard Comfort
	VWR	NITRILE Light
Pipette tips	Biozym	SurPhob; 20, 200, 1000 µL
		Safe Seal SurPhob; 20, 200, 1000 µL
Reaction tubes	Sarstedt	0.2, 0.5, 1.5, 2.5 mL
Syringes	Braun	5, 10, 25 mL
Reaction columns	Intavis	5 mL
Well plates	Starstedt	TC Plate 24 Well Standard F
	ibidi	8 Well Chamber, removable
Coverslips	Hartenstein	Microscope Cover Glasses 24 x 60 mm
Microscope Slides ISO 8037/1	Thermo Scientific	AGAA000001#02E
	Marienfeld	1000612
Test Tube 13x75 mm 5 mL	VWR	216-1167

2.5 Software

Software used within this thesis in order to perform experiments, data interpretation and figure design is listed in Table 7.

Table 7 List of software used.

Software	Reference
Chemdraw	http://www.perkinelmer.com/category/chemdraw
Fiji	http://fiji.sc
Microsoft Office	https://products.office.com
MultiPep	Intavis
OpenLab Chemstation	Agilent Technologies
Inkscape	https://inkscape.org
PyMOL	https://pymol.org
Python V3.9.4	https://www.python.org
python-bioformats V1.5.2	https://github.com/CellProfiler/python-bioformats/

R	https://www.r-project.org
scikit-image V0.18.1	https://scikit-image.org
scikit-learn V1.1.1	https://scikit-learn.org
scipy V1.7.3	https://scipy.org
seaborn V0.11.1	https://seaborn.pydata.org
Xcalibur	Thermo Scientific

3 Methods

An overview of the methods used within the iterative process of probe design and evaluation is presented in Figure 4.

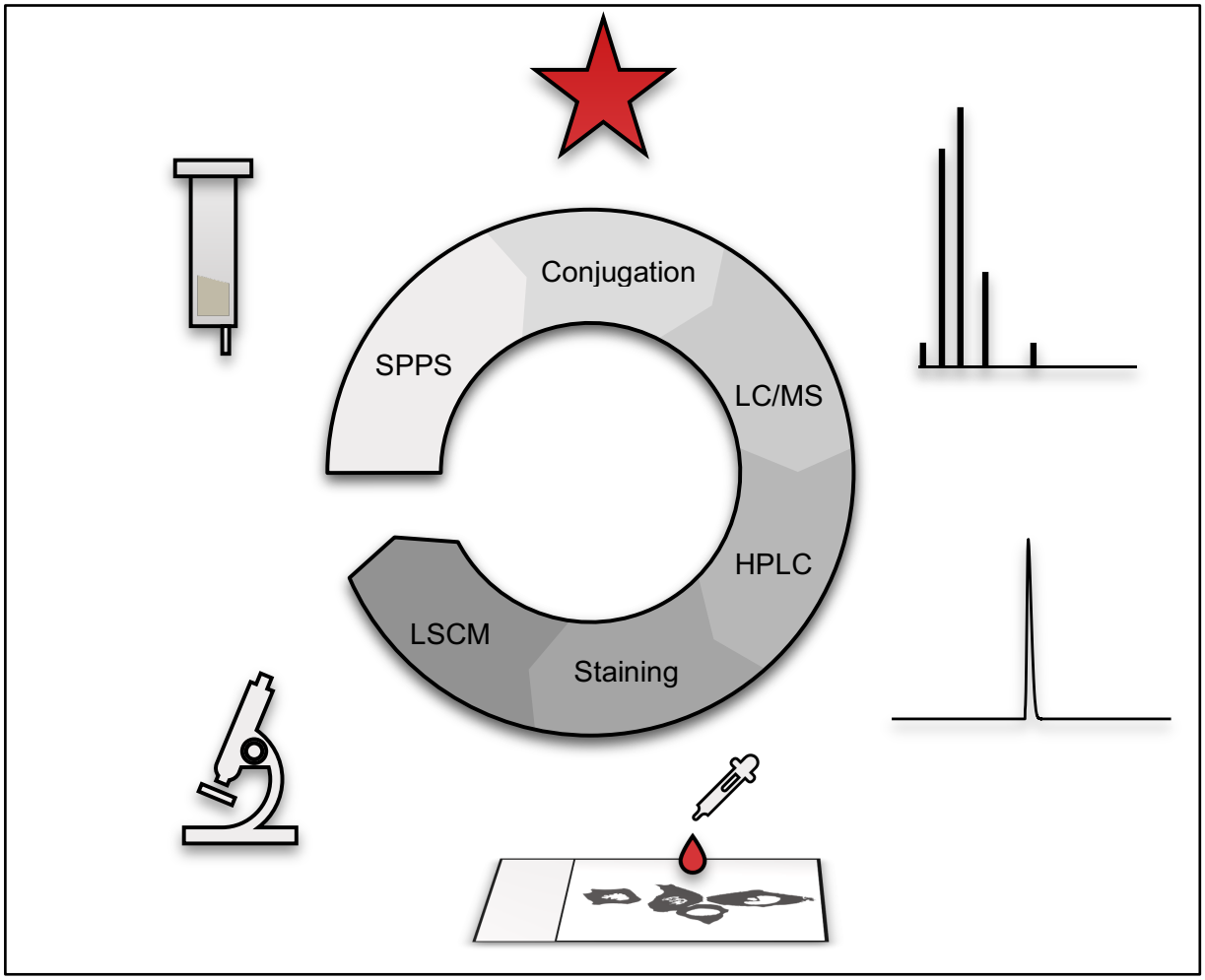

Figure 4 Workflow for peptide probe synthesis and evaluation. First, the peptide is synthesised using SPPS techniques. The compound is then conjugated to a fluorescent dye of choice and synthesis is confirmed by LC/MS. Now the probe is purified and HEK cells expressing the fluorescent target protein are subsequently stained. Laser scanning confocal microscopy (LSCM) is performed, and the staining is evaluated.

3.1 Automated Solid Phase Peptide Synthesis

Peptides were manually or automatically synthesised using a MultiPep RSi robot (Intavis). Peptide synthesis in milligram-scale was achieved using 100 mg 2-chlorotrityl chloride resin (theoretical load of 1.6 mmol/g, thus corresponding to a molar synthesis scale of 160 µmol).

3.1.1 Resin Loading

The resin was swollen in 2 mL dry dicloromethane (DCM) for 30 minutes (min). It was then manually loaded with the most C-terminal amino acid of the desired peptide chain (1 eq) and the orthogonally protected Boc-Gly-OH (1 eq) to reduce resin loading in order to prevent aggregation of the growing peptide chain. DIEA (2 eq) was added. The reaction was performed under dry conditions in dry DCM for 12 h. Thereafter MeOH was added to the reaction mixture for 1 h to perform resin capping. Now the resin was washed with 3x DMF, 3x DCM and 3x DMF. The deprotection step of the amine was performed twice with 20% Pip in DMF for 10 min each. The filtrate was collected and the absorption of the dibenzofulvene–piperidine adduct was determined (Extinction coefficient obtained from the literature $\varepsilon_{289.8nm} = 6089 \frac{L}{mol * cm}$ [43]). The concentration c $[\frac{mol}{L}]$ can be calculated according to Labert-Beer's law with the absorption A [dimensionless unit], the extinction coefficient $[\frac{L}{mol * cm}]$ and the pathlength [cm]

Equation 6 Labert-Beer's law

$$c = \frac{A}{\varepsilon l}$$

3.1.2 Peptide-Chain Elongation

For peptide-chain elongation the loaded resin was transferred to the MultiPep RSI robot (Intavis). For the protocol used for peptide-chain elongation refer to Table 8. Capping solution: 0.5 M acetic anhydride, 0.5 M DIEA in 1-methyl-2-pyrrolidon (NMP) (all v/v). Coupling solution: 0.25 M N,N'-diisopropylcarbodiimide (DIC), 0.25 M ethyl cyanohydroxyiminoacetate (oxyma), 0.25 M derivative. After the last derivative was added to the peptide-chain, the protocol mentioned in Table 9 was used to prepare the product for cleavage.

Table 8 Automated SPPS coupling cycle.

No.	Action	Reagent	Solvent	Vol. [mL]	Time [min]	Repeats
1	Deprotection	20% Pip	DMF	2	10	2
2	Wash		DMF	7		6
3	Extract				0.5	
4	Coupling	Coupling Solution	DMF	2	90	
5	Extract		-		0.5	
6	Wash		DMF	7		1
7	Coupling	Coupling Solution	DMF	2	90	
8	Wash		DMF	7		1
9	Extract		-		0.5	
10	Coupling	Coupling Solution	DMF	2	90	

11	Wash		DMF	7		3
12	Capping	Capping Solution	NMP	2.5	30	
13	Wash		DMF	7		6
14	Extract				0.5	

Table 9 Manual SPPS Preparation for Cleavage.

No.	Action	Reagent	Solvent	Vol. [mL]	Time [min]	Repeats
1	Wash	-	DMF	3		3
2	Wash	-	DCM	3		3
3	Wash	-	DMF	3		3
4	Wash	-	DCM	3		3

3.1.3 Cleavage and Work-up

Cleavage of the peptide from the solid support was performed simultaneously with the cleavage of the protection groups from the side chains. The cleavage solution (Modified Reagent K: 82.5% trifluoroacetic acid (TFA), 5% phenol, 5% H_2O, 5% thioanisole, 2.5% ethane-1,2-dithiol (EDT) [all v/v]) was freshly prepared. Cleavage was performed for 4 h at room temperature (RT) with 2.5 mL of cleavage solution per vial. The crude product was precipitated by incubation in ice cold ether at -20 °C overnight. The mixture was centrifuged (4500 g, 4 °C, 10 min) and the supernatant was discarded. The crude product was resuspended in ether, centrifuged (4500 g, 4 °C, 10 min) and the supernatant was discarded. This step was repeated twice. After evaporation of the solvent, the crude was dissolved in 10 mL of 50% acetonitrile in H_2O (v/v), flash frozen in liquid N_2 and lyophilised. The crude product was obtained as a *white powder* and purified with reverse phase high performance liquid chromatography (HPLC). Liquid chromatography-mass spectrometry (LCMS) confirmed the success of the synthesis.

3.2 Fluorophore Conjugation

Fluorescent dyes suitable for click chemistry either with N-hydroxysuccinimide (NHS) or a maleimide group were bought from Lumiprobe and Thermofisher as a lyophilised powder. Either NHS conjugation or maleimide conjugation was performed.

3.2.1 NHS Conjugation

The peptide was dissolved in 100 µL of dry DMF in a 1.5 to 3-fold excess. Dry DIEA and the fluorescent dye was added. NHS-conjugation was performed overnight in DMF at 4 °C while shaking (Eppendorf, Thermo Mixer C, 650 rpm). The solvent was removed under reduced

pressure and the product was resuspended in 20% MeCN in H_2O (v/v) and purified using HPLC. LCMS confirmed the success of the conjugation.

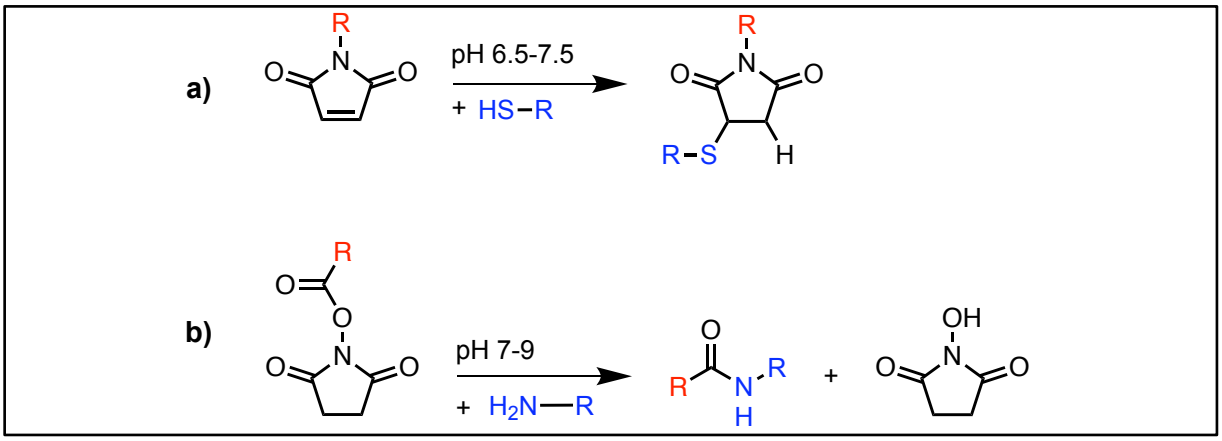

Figure 5 Reaction mechanism for two fluorophore-peptide conjugation strategies. **a)** Is a schematic of a thiol-maleimide Michael Addition and **b)** represents NHS labelling. R specifies the fluorescent dye whereas the peptide is specified by R.

3.2.2 Maleimide Conjugation

For maleimide conjugation a thiol-maleimide Michael Addition was performed. Conjugation was either performed in phosphate buffered saline (PBS) or DMF.

3.2.2.1 Labelling in PBS

The peptide was dissolved in 200 µL freshly prepared 1xphosphate-buffered saline (PBS) (pH = 7.0) and provided in a 1.5 to 3-fold excess. 1 mg fluorescent dye was dissolved in 100 µL DMSO. Since the peptide was provided in excess and checked for oxidation in LCMS prior to labelling, no reducing agents were added. The conjugation was performed under oxygen-free conditions overnight at 4 °C while shaking (Eppendorf, Thermo Mixer C, 650 rpm). The solvent was removed under reduced pressure and the product was resuspended in 20% MeCN in H_2O (v/v) and purified with HPLC. LCMS confirmed the success of the conjugation.

3.2.2.2 Labelling in DMF

The peptide was dissolved in 100 µL DMF. 1 mg fluorescent dye was dissolved in 10 µL DMF. The conjugation was performed under oxygen-free conditions overnight at 4 °C while shaking (Eppendorf, Thermo Mixer C, 650 rpm). The solvent was removed under reduced pressure and the product was resuspended in 30% MeCN in H_2O (v/v) and purified with HPLC. LCMS confirmed the success of the conjugation.

3.3 Spectrophotometry

Absorption of the fluorescently labelled samples was calculated based on the following extinction coefficients provided by Lumiprobe.

Table 10 Extinction coefficients used for spectrophotometry measurements.

Fluorescent Dye	**Extinction Coefficient ε $\left[\frac{1}{M \cdot cm}\right]$**	**Wavelength$_{ex}$ [nm]**
Cy5	250 000	650
Alexa Fluor 647	239 000	650
Sulfo-Cyanine 5	270 000	646

3.4 Liquid Chromatography

Reverse phase HPLC was performed on instruments/columns specified in Table 11.

Unless otherwise noted, buffers used in HPLC and LCMS were composed of (all v/v):

- HPLC
    - Buffer A: 95% H_2O, 5% MeCN, 0.1% TFA
    - Buffer B: 95% MeCN, 5% H_2O, 0.1% TFA
- LCMS
    - Buffer A: 95% H_2O, 5% MeCN, 0.1% FA
    - Buffer B: 95% MeCN, 5% H_2O, 0.1% FA

UV-absorption was detected at 210 and 254 nm.

Table 11 Liquid chromatography systems used.

Type	**Source**	**Product Name**	**Columns used**
Semi-preperative HPLC	Thermo Fisher	UltiMate 3000	Onyx™ Monolithic Semi-PREP C18, LC Column 100 x 10 mm, Thermo Scientific Hypersil GOLD, 5µm, 150 x 4.6 mm
Analytical HPLC	Shimadzu	Prominence	Onyx™ Monolithic C18, LC Column 100 x 4.6 mm
LCMS	Agilent	Infinity II/ InfinityLab LC/LCMSD	Onyx™ Monolithic C18, LC Column 50 x 2 mm

3.5 Cell Culture

This section describes methods employed to culture, transfect and fix human embryonic kidney 293T cells (HEK293T cells).

3.5.1 Cell Cultivation and Storage

HEK293T cells were grown in Dulbecco's Modfied Eagle Medium (DMEM) with 10% fetal bovine serum (FBS) and 1% L-glutamine under permanent selection with penicillin and streptomycin (1%) at 37°C and 5% CO_2. Cells were supplemented with GlutaMax and pyruvate (GIBCO). Stable HEK293 cells expressing eGFP-gephyrin were grown under the selective antibiotic G418 at a concentration of 0.4 mg/mL.

eGFP-gephyrin expressing cells were plated on coverslips coated with 35 µg/ml Poly-D-Lysine in an 8-well plate.

3.5.2 Transfection of HEK293T cells

Transfection was performed at 60-80% confluency. DMEM was changed prior to transfection. The DNA (1 µg) was added to 100 µl DMEM and mixed. 4 µl fresh polyethylenimine (PEI) (1 mg/ml) was added, mixed an incubated for 20 min at RT. The transfection mix was added dropwise on the cells while swirling and incubated overnight. The medium was exchanged to fresh DMEM and 2% FBS after 12-24 h. cDNA expression construct was kindly supplied by Prof. Matthias Kneussel (ZMNH, Hamburg, Germany) [44, 45]. Cells were subsequentially fixed and stained according to the protocols mentioned in subsection 3.6.

3.6 Fixation Methods

This subsection lists different fixation methods used in this thesis.

3.6.1 Methanol Fixation

The protocol for MeOH fixation is specified in Table 12. For multiple probes, steps no. 5 and 6 are repeated.

Table 12 Protocol for MeOH fixation. Volume (Vol.) specified for each chamber. Protocol provided by Vladimir Khayenko, AG Maric, Würzburg.

No.	Action	Derivative	Vol. [µl]	Time [min]	Repeats
1	Washing	PBS	250		3
2	Fixing	MeOH	250	5	
3	Washing	PBS	250		3
4	Blocking	2% BSA in PBS	250	60	
5	Washing	PBS	250		3
6	Staining	Probes in 0.1% BSA	250	90	
7	Washing	PBS	250		3
8	Drying			10	
9	Mounting	Mowiol	12		

3.6.2 Paraformaldehyde Fixation

The PFA fixation is specified in Table 13. For multiple probes, steps no. 9 and 10 are repeated.

Table 13 Protocol for PFA fixation. Volume specified for each chamber. Protocol from Natascha Schäfer, AG Villmann, Würzburg.

No.	Action	Derivative	Vol. [µl]	Time [min]	Repeats
1	Washing	PBS	250		3
2	Fixing	4% PFA, 4% Sucrose in PBS	250	15	
3	Washing	PBS	250		3
4	Blocking	50 mM NH_4Cl	250	10	
5	Washing	PBS	250		1
6	Quenching	0.1 mM Glycine	250	15	
7	Washing	PBS	250		1
8	Blocking, Permeating	2% BSA, 0.1% Triton X-100 in PBS	250	30	
9	Washing	PBS	250		3
10	Staining	Probes in 0.1% BSA	250	90	
11	Washing	PBS	250		3
12	Drying			10	
13	Mounting	Mowiol	12		

3.6.3 Glyoxal Fixation

The protocol for glyoxal fixation is specified in Table 14. For multiple probes, steps no. 6 and 7 are repeated. Blocking buffer = 2.5% bovine serum albumin (BSA), 0.1% Triton X-100 in PBS. Glyoxal was freshly prepared according to the protocol provided by Richter et al. [46].

Table 14 Protocol for glyoxal fixation. Volume specified for each chamber. Protocol by Vladimir Khayenko, AG Maric , Würzburg.

No.	Action	Derivative	Vol. [µl]	Time [min]	Repeats
1	Washing	PBS	250		3
2	Fixing	Glyoxal	250	60	
3	Washing	PBS	250		3
4	Quenching	100 mM NH_4Cl	250	30	
5	Washing	PBS	250		3
6	Blocking, Permeating	Blocking buffer	250	15	
7	Staining	Probes in blocking buffer	250	90	
8	Washing	Blocking buffer	250		3
9	Washing	500 mM NaCl in H_2O	250		
10	Washing	PBS	250		2
11	Drying				2
12	Mounting	Mowiol	12		

3.7 Microscopy

Microscopic images were taken at the Imaging Facility of the Rudolf Virchow Center with a Leica TCS SP5 confocal laser scanning microscope. The HCX PL APO lambda blue 63.0x1.40 OIL object was used for image acquisition. Immersion oil Immersol 518 F (Zeiss) with a refractive index of 1.5180 at 23 °C was used. Metadata from image acquisition is presented upon request.

3.8 Figures

3.8.1 Boxplots

If not specified otherwise, numerical axis is in linear scale. Boxplots shown indicate the three quartile values as horizontal lines. Data within the 1.5 interquartile range of the lower and upper quartile are represented as “whiskers”. Data falling outside of the 1.5 interquartile range are depicted using individual markers.

3.8.2 Microscopic images

Microscopy images are presented as a superimposed image of the fluorescent signal on the brightfield signal. In order to increase visibility of fluorescent image data, images are inverted [47]. A brighter colour is mapped to a low signal whereas a high signal is represented by a darker colour. Unless otherwise noted, Look-Up Tables (LUTs) are normalised for each figure.

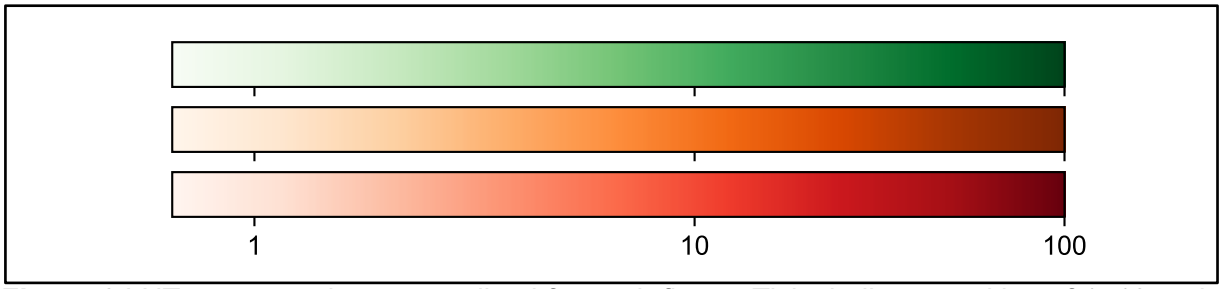

Figure 6 LUTs presented are normalised for each figure. Ticks indicate position of 1, 10 and 100% of normalised signal intensity. x-axis in logarithmic scale.

4 Results and Discussion

4.1 Project Aims

The first goal of this project was the synthesis of three monovalent and dimeric fluorescent peptide probes in milligram scale at purities exceeding 95%. The second goal was to establish a high-throughput assay for the evaluation of resulting probes.

4.2 Probe Design

Maric et al. demonstrated that monovalent peptides targeting gephyrin E-domain (gephE) can be used for visualisation of gephyrin when combined with fluorescent dyes [30]. The application of these probes, however, was limited by their intermediate affinity and low signal-over-noise ratio. Application of these probes in primary neurons resulted in incomplete staining of native gephyrin and necessitated the use of related peptide variants as specific blocking agents. Additionally, these probes were not compatible to super-resolution approaches such as direct STORM. To improve specificity, signal-over-noise and binding efficiency I exploited the possibility to enhance probe affinity by dimerization [30, 48, 49]. Maric et al. 2014 achieved cross-linking of the C-terminal Cysteines with a bismaleimide-activated polyethylene glycol (peg) compound BM(peg)2 as shown in Figure 7a [49]. My synthesis strategy achieves dimerization via a Fmoc-Lys(Fmoc)-OH as shown in Figure 7b. Major advantages of this dimeric architecture are:

- direct and efficient synthesis of dimeric peptide without the need of purification before the dimerization
- modular and flexible incorporation of numerous commercially available building blocks allow for the optimisation of the dimeric architecture
- compatible to common SPPS and even automated SPPS synthesis methods
- allows for facile and stoichiometric functionalisation and at the resulting C-terminal handle

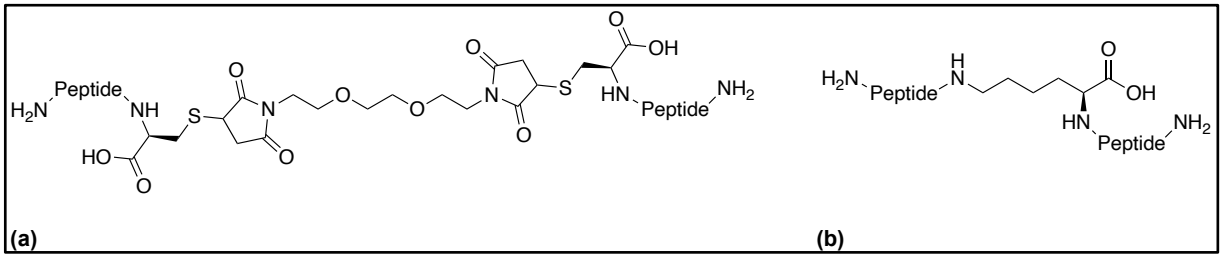

Figure 7 Two chemical structures of compounds that allow for multivalent peptide synthesis strategies. **(a)** shows the BM(peg)2 dimerization strategy while **(b)** represents the Fmoc-Lys(Fmoc)-OH dimerization dimerization strategy.

4.3 Binding Sequence

The binding sequence is derived from the GlyR-β subunit/gephyrin interaction site. It was chosen based on data from peptide-array-based mutational scans for the GlyR-β subunit residues ^{397}D–F^{408} by Maric et al. [30]. The core binding motive ^{392}DLRSNDFSIVGSLPR^{406} was tested by Clemens Schulte (AG Maric) for binding to native gephyrin within mouse brain lysate (*see* Supplementary Figure 1) [50]. These data represented the chemical space for possible modifications by identifying which amino acids are tolerated at each position of the peptide probe. Hydrophilic amino acids were favoured in order to increase hydrophilicity of the peptide probe. This rationale let me choose YSIVGSYPR as binding sequence.

4.4 Linker Region

The linker region was systematically optimised by measuring EC_{50} values in peptide microarray format for linkers of different sizes as shown in Supplementary Figure 2 and truncated, dimeric versions of the GlyR-β sequence ^{398}FSIVGSLP^{405}. Overall, the length of the binding sequence appears to be more important for gephE binding compared to the linker length. Interestingly, the mutated and more hydrophilic peptide YSIVGRYPK* shows higher sensitivity in terms of a lower EC_{50} value compared to the dimeric wild type (WT)-sequence. The dimeric probe in this project uses the polyethylene glycol (peg) derivative Fmoc-O2Oc-OH building block as a linker as shown in Figure 8. Pegylation of peptides is a way to modulate peptide pharmacokinetics: In a review by Mäde et al. the peg motive is reported to be ”amphiphilic, non-toxic, little immunogenic, non-antigenic and highly soluble” [51]. In the same review it is reported that every ethylene oxide unit binds 3 H_2O molecules which increases solubility of the pegylated peptide compound. This water shield would further hinder antibodies and proteases from binding and thus reduce antigenicity and increase stability of the compound *ibid*. In order to combine the benefits of the pegylated peptide with a small displacement of the fluorescent dye in case of C-terminal labelling, the relatively small linker 6K* was used (*see* Supplementary Figure 2).

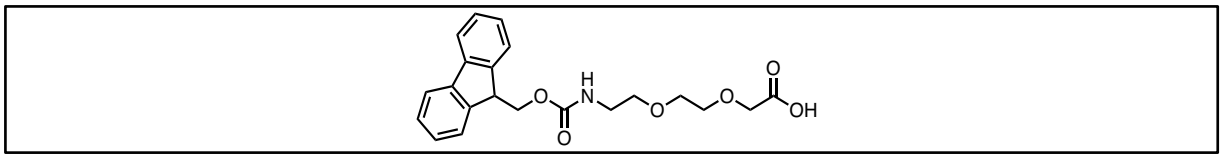

Figure 8 Structure of Fmoc-O2Oc-OH.

4.5 Fluorophore

Several requirements for the fluorescent dye must be fulfilled. The fluorescent dye of choice must be:

- suitable for click chemistry
- as hydrophilic as possible in order to prevent the dye interacting with the membrane [12]
- suitable for super-resolution microscopy
- yield a high photon count for high contrast

These rationales let me choose the fluorescent dyes mentioned in Table 10 for further evaluation. N-terminal as well as C-terminal labelling was performed as shown in Figure 5.

4.6 Solid Phase Peptide Synthesis

Solid phase peptide synthesis was performed according to section 3.1.

4.7 Monomeric Peptide Synthesis

Considering the data mentioned in subsection 4.2, a peptide with the binding sequence and linker YSIVGSYPRpegC was constructed. 2-Chlorotrityl chloride resin (100 mg) was swollen for 30 minutes in dry DCM prior to loading. Fmoc-L-Cys(Trt)-OH (0.16 mmol, 1 eq, 94 mg) and Boc-Gly-OH (0.16 mmol, 1 eq, 28 mg) were dissolved in dry DCM and resin was loaded. Resin loading was calculated to be 0.4 $\frac{\text{mmol}}{\text{g}}$ according to Labert-Beer's law. The peptide was then transferred to the peptide synthesizer (Intavis MultiPep RSi) for automated peptide chain elongation. In the following step, the peptide was manually cleaved and prepared for purification by dissolving the crude product in 20 MeCN and 80% H_2O. Success of the synthesis was determined by LC/MS. Purification of ≥ 95% was performed with preparative HPLC. The product was then flash frozen, lyophilised and stored at -20 °C.

4.8 Dimeric Peptide Synthesis

The dimeric peptide $(YSIVGSYPRpeg)_2K*C$ was rationally designed according to the data presented above. Peptide synthesis was performed as described before with a resin loading of 0.48 $\frac{\text{mmol}}{\text{g}}$ according to Labert-Beer's law and equals. The following steps were performed with the protocol mentioned in subsection 4.7.

4.9 Fluorophore Conjugation

For conjugation with Sulfo-Cyaninine-5-maleimide, the lyophilised dimeric peptide (3 mg, 1.2 µmol) was dissolved in 1xPBS (200 µL, pH 7). Sulfo-Cyaninine-5-maleimide in dimethyl sulfoxide (DMSO) was added (38.5 µL of 0.125 $\frac{\text{mmol}}{\text{mL}}$, 0.48 µmol). 60 µL DMSO were added to the mixture. Reaction was performed while shaking (Eppendorf, Thermo Mixer C) for 18 h at 4 °C (650 rpm). After the first purification with HPLC, yield was 0.968 mg (0.29 µmol). After a second purification cycle, yield of the dimer was reduced to 0.42 mg (0.14 µmol) .

For conjugation with Sulfo-Cyaninine-5-maleimide (sCy_5), lyophilised monomeric peptide (1.77 mg, 1.4 µmol) was dissolved in 1xPBS (200 µL, pH=7.0). Sulfo-Cyaninine-5-maleimide in DMSO was added (61.5 µL of 0.125 $\frac{\text{mmol}}{\text{mL}}$, 0.77 µmol). 60 µL DMSO were added to the mixture. Reaction was performed while shaking (Eppendorf, Thermo Mixer C) for 18 h at 4 °C (650 rpm). After two purification cycles, yield the monomer was 0.62 mg (0.3 µmol).

For conjugation with Alexa Fluor™ 647 C_2, lyophilised dimeric peptide (3 mg, 1.2 µmol) was dissolved in 1xPBS (200 µL, pH 7.4). The amount of Alexa Fluor™ 647 C_2 maleimide added was < 1 mg. Alexa Fluor™ 647 C2 maleimide was dissolved in 100 µL PBS. 100 µL DMSO was added to the mixture. The reaction was performed while shaking (Eppendorf, Thermo Mixer C) for 18 h at 4 °C (650 rpm). The crude product was subsequently purified. Several purification steps have been performed to reach a pure compound. Yield after first purification was 1.31 mg (0.36 µmol) but purity was <95%. Yield after final purification was 56.7 µg with a purity of 95%. Yield of the dimeric peptide was determined by spectrophotometry (NanoDrop ND1000) with $\varepsilon_{650\ nm}$=270 000 $\frac{\text{L}}{\text{mol}\cdot\text{cm}}$.

Table 15 Peptide probes synthesised and tested.

Name	Valency	N-terminal Fluorescent Dye	Binding Sequence	Linker	C-terminal Fluorescent Dye	Molecular Weight [g/mol]
$NN1D_A$	Dimer		YSIVGSYPR	pegK^*C	Alexa Fluor™ 647 C_2	3569.11
$NN1D_C$	Dimer		YSIVGSYPR	pegK^*C	Sulfo-Cyanine-5	3391.55
$NN1M_C$	Monomer		YSIVGSYPR	pegC	Sulfo-Cyanine-5	2090.82
$_C$VK14	Monomer	Sulfo-Cyanine-5	YSIVGSYPR	RRRRRRRR		2572.15

4.10 Microscale Thermophoresis

In order to quantify GephE binding for the peptide probes synthesised, MST and TRIC was performed. MST assays performed by Clemens Schulte (AG Maric).

A concentration of 11nM $NN1D_C$ was titrated with GephE at a dilution series of 1:2 and a starting concentration of 12.5 µM. MST measurements were performed with a Monolith NT.115 pico system (Nanotemper). A K_D of 538.69 nM could be determined after sigmoidal fitting of the curve (4PL-regression, *scipy*). The affinity measured is one order of magnitude lower as the original, truncated GlyR β WT peptide (^{398}FSIVGSLPRDF^{408}) with a K_D of 8.3 µM. It is several orders or magnitude lower compared to the $GABA_AR$ α3 WT (^{368}FNIVGTTYPIN^{378}) with a KD of 190 µM [52]. However, these measurements were performed in ITC, thus values are not directly comparable to the MST measurements.

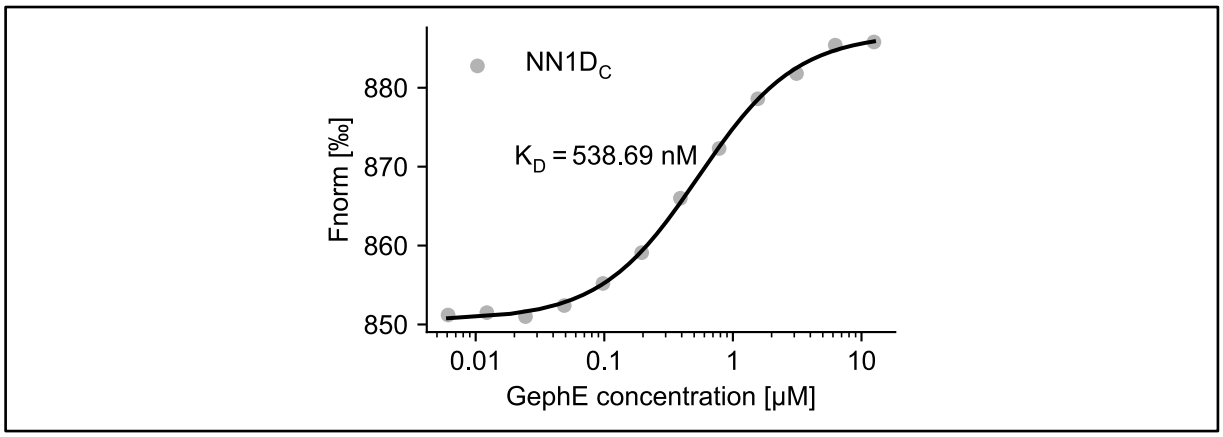

Figure 9 Binding of $NN1D_C$ to GephE is confirmed by MST.

In order to evaluate the impact of the fluorescent dye on the K_D, NN1D was conjugated to Alexa Fluor™ 647 C_2 as described before. TIRC Measurements were performed on Dianthus NT23.PicoDuo (Nano- temper Technologies GmbH). For detailed methods refer to Schulte et al, iScience 2021 [50].

The probe $NN1D_A$ is titrated with unlabelled gephE (*see* Figure 10a) in TRIC. F_{norm} was measured according to Equation 5. The obtained dose-response curve was fitted using 4PL equation and a K_D of 1.54 nM could be determined.

In a next step, gephE and $NN1D_A$ at a nanomolar concentration were preincubated thus forming a peptide-protein complex. This complex is than titrated with competitor peptides, and displacement of $NN1D_A$ by unlabelled peptides (NN1D, NN1M and a nonbinder) can be observed. This displacement is seen as an inverse TRIC signal as shown in Figure 10b and the known binding hierarchy of a monomeric vs a dimeric peptide probe could be reproduced [49, 50].

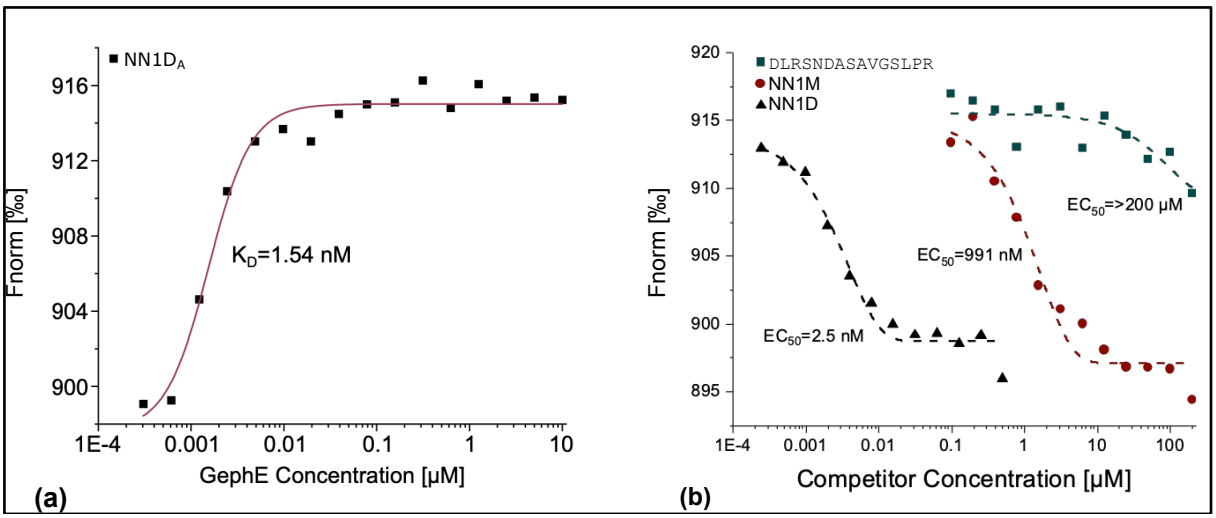

Figure 10 TIRC binding curves for fluorescently labelled and unlabelled peptide probes. **(a)** NN1D$_A$ shows low nanomolar affinity towards unlabelled gephE. **(b)** A NN1D$_A$-gephE complex is titrated with competitor peptides. The dimeric NN1D shows lowest EC_{50} value (2.5 nM) indicating higher affinity to gephE compared to the monomeric NN1M and a nonbinder (DLRSNDASAVGSLPR). Reproduction of figure 2 in Schulte et al. (iScience, 2021) [50].

This setup allows for accurate, quasi-label-free affinity, parallel affinity measurements of molecules targeting gephE with minimal sample consumption.

Interestingly, K_D reported for NN1D$_A$ was 350 times lower compared to NN1D$_C$. However, MST and TIRC measurements are not directly comparable to each other as they were performed on different machines. For microscopy however, we continued experiments with Sulfo-Cyanine5 maleimide (sCy5) because of two reasons: First, because of economic reasons as 5 mg sCy5 was 275 € (55 $\frac{€}{mg}$) compared to 1 mg of Alexa Fluor™ 647 C_2 maleimide at 545 € (545 $\frac{€}{mg}$) at the time of purchase. Second, separation using HPLC for NN1D$_C$ had higher yields, as NN1D$_A$ and the unconjugated NN1D had close to overlapping retention times in our HPLC setup, even with time consuming (>30 min per run) isocratic and gradient elution protocols.

4.11 Microscopy

4.11.1 Staining of Gephyrin in HEK293T-Cells

A cellular assay was established to evaluate specificity and sensitivity of the synthesised probes. Fixed eGFP-gephyrin expressing HEK293T cells (GephHEK) were stained with the peptide probes. Fluorescence microscopic data were acquired using laser scanning confocal fluorescence microscopy (LSCM) according to subsection 3.7.

Upon excitation, eGFP-gephyrin expressing HEK293T cells (GephHEK) show two distinct cellular regions (region of interest ROI) that can be differentiated based on their signal intensity. Whilst a low signal intensity is attributed to the cellular eGFPgephyrin (ROI_C), a higher signal-to-noise ratio (SNR) is given by cytosolic eGFP-gephyrin aggregates, earlier referred to as blobs (ROI_B) [45, 53]. Thus, the cells can be segmented in two regions based on their signal intensity in the eGFP-channel.

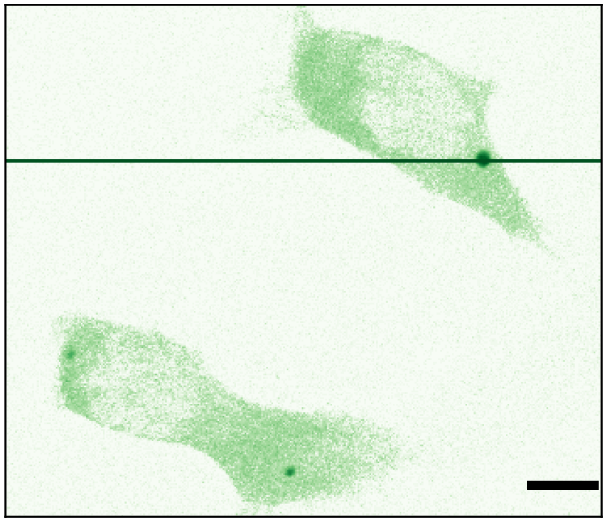

(a) Raw Image

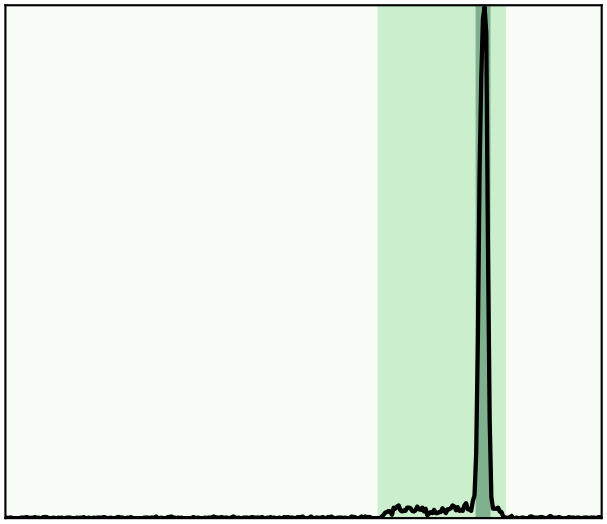

(b) Normalized Intensity

Figure 11 Inhomogeneous gephyrin distribution in GephHEK. **(a)** shows the raw image with a cutting line through the image. **(b)** shows the normalized intensity on a linear y axis for each pixel in the cutting line on a linear scale. The different ROIs are depicted as different shades of green Scale bar = 10 µm.

4.12 Automated Image Segmentation

Analysis of the microscopic images was performed with a custom-built image analysis pipeline. Thus, image segmentation could be automated which leads to an increased reproducibility of the results and faster image segmentation of large datasets with up to 100 microscopic images.

All blurring and thresholding functions were used from the python project *scikit-image* [54]. *python-bioformats* was used to read LEICA .lif files. Image segmentation was performed based on the eGFP-channel.

The image processing pipeline is structured as follows: The raw image (Figure 13a) is blurred using a gaussian blur in order to eliminate high frequency noise (Figure 13b). Based on the image's histogram, Yen's thresholding method is applied (Figure 12). This results in a

segmentation of the gephyrin blobs and the rest of the image. In order to subtract the background from the cell, the image without the gephyrin blobs is blurred again (Figure 13c) and Otsu's thresholding method is applied which allows for even further image segmentation (Figure 12). The final mask is shown in (Figure 13d). Both, Yen's and Otsu's thresholding functions are automatic, histogram-based thresholding functions used in traditional computer vision. Manual input is needed for the standard deviation of the gaussian kernel for the blurring functions. All segmentations were visually checked for plausibility in order to ensure data quality.

The integrated intensity as the pixelwise sum of all intensities was calculated pixelwise for all ROIs in each channel. In a next step, probe signal in den sCy5-channel was normalised to the GFP-signal.

Equation 7 Normalized Intensity

$$\text{Normalized Intensity} = \frac{\text{Cyanine5}}{\text{eGFP}}$$

The code for the image segmentation pipeline can be provided upon reasonable request.

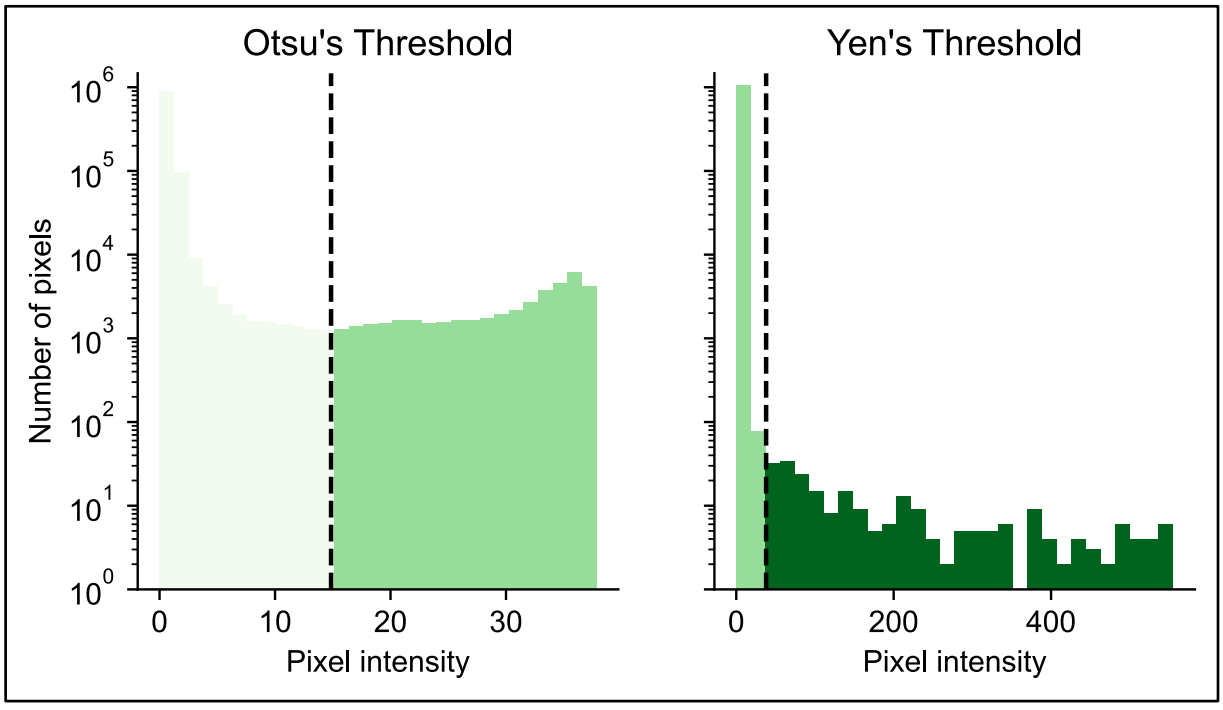

Figure 12 Example of automated thresholding functions. Otsu's threshold displayed on the left as a dashed line. Light green ROI_N, green ROI_C. Yen's Threshold depicted on the right segmenting ROI_B (dark green) from ROI_{C+N} (green). Number of pixels for image of size 1024x1024 .

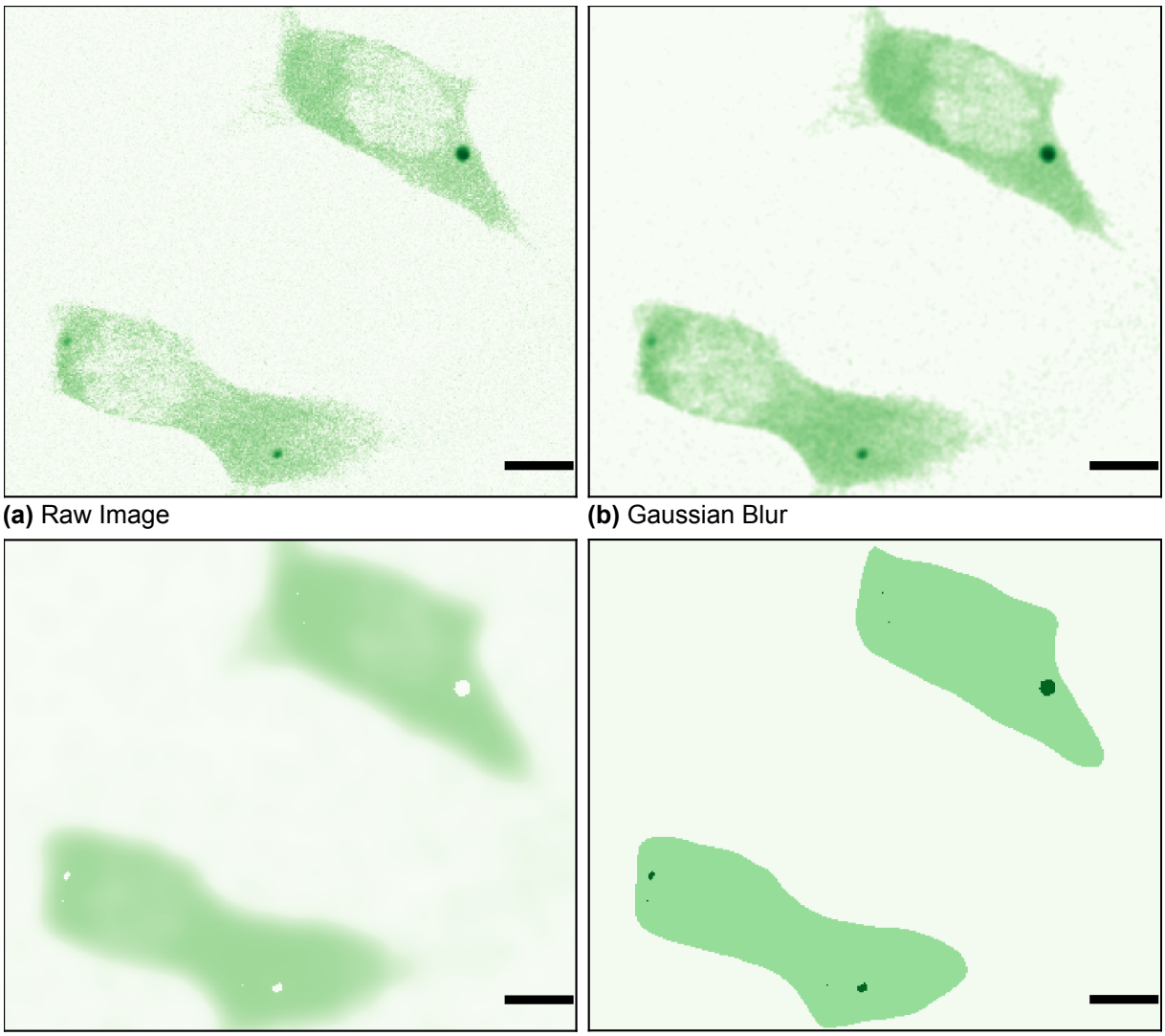

(a) Raw Image **(b)** Gaussian Blur

(c) Gaussian Blur **(d)** Segmented Image

Figure 13 Image segmentation pipeline for GephHEK cells. **(a)** shows a section of a raw microscopic image acquired for GephHEK. eGFP-gephyrin blobs are clearly visible as dark green dots (n=3). **(b)** shows the first blurring step. The ROI_B are subtracted from the image and the image is blurred again **(c)**. **(d)** shows the mask created for the three ROIs. ROI_N in light green, ROI_C in green and ROI_B in dark green. Scale bar = 10 µm.

Table 16 Segmentation of fluorescent image in multiple ROIs.

Name	Region	GFP signal intensity	Colour
ROI_B	eGFP-gephyrin aggregates (blobs)	high	dark green
ROI_C	cellular eGFP-gephyrin without ROI_B	medium	green
ROI_N	Background, Image without ROI_B and ROI_C	low	light green

4.13 Evaluation of Staining Properties of Peptide Probes

In order to evaluate staining properties of different peptide probes, several assumptions had to be made. First, the eGFP-signal is considered as true positive in terms of sensitivity analysis. Second, cells that do not express eGFP-gephyrin were considered true negatives for qualitative analysis. For quantitative analysis it was assumed, that labelling of different cellular ROIs is linear. Thus, a constant labelling ratio was assumed as a true negative signal in terms of specificity analysis.

4.13.1 Dose-response Relationship in gephHEK with MeOH Fixation

$NN1D_C$ was directly compared against is monovalent, equally labelled counterpart $NN1M_C$.
Probe concentrations stock solution of 2.4 µmol ($NN1D_c$) and 2.5 µmol ($NN1D_M$) were prepared using spectrophotometry (*see* section 3.3). A serial dilution with a dilution factor of 3 was prepared for both compounds. The stock solutions were diluted and probe concentrations of 52 nM; to 0.07 nM were prepared**.** The cells were prepared for the assay as mentioned in subsection 3.5.2. Fixation was performed with MeOH as specified in Table 12. After staining, cells were stored for 18h at 4 °C.
For LSCM evaluation of the probes, the lasers and detectors were adjusted for the highest concentration of $NN1D_C$ to yield roughly the same intensity for the GFP and the Cyanine5 channel. The HyD detector (photon multiplier mode) was used for increased sensitivity. Gain was set 397. Five images per probe and concentration were recorded at 8-bit (0-255) at different sample locations. Image size was 512x512 pixels. Intensity values in the Cyanine5 channel were normalized pixelwise to the intensity values in the GFP channel. Scan speed was set to100 Hz.
The HCX PL APO lambda blue 63.0x1.40 OIL UV object with a numerical aperture of 1.4 was used for image acquisition. Excitation of GFP was achieved with 458 nm argon laser. Excitation of the peptide probe was achieved with 633 nm HeNe laser. HyD filter settings for GFP signal detection were set to 500-552 nm. sCy5 signal was detected at 657-729 nm. 5 images were acquired for every concentration at different sample locations (80 in total). Images were automatically segmented as described earlier. Throughout the experiment microscopic settings were kept constant.
Microscopic images were automatically segmented as described in subsection 4.12. ROI_B with a pixel count of 15 and higher as well as ROI_C with a pixel count of 150 and higher were included in the analysis. ROIs, that had saturated pixels with a value of 255 in the eGFP or Cyanine5 channel were excluded from the analysis.

Descriptive statistics of the ROI detection is presented in Table 17. More ROI_C compared to ROI_B could be included in the analysis due to the filtering rules applied. Thus, more ROI_B had to be excluded from analysis due to presence of saturated pixels.

Table 17 Number of ROIs for each concentration included in analysis for gephHEK with MeOH as fixative. Descriptive statistics (min, max, mean, median) for number of ROIs detected.

ROI	Probe	min	max	mean	median
ROI_B	$NN1M_C$	15	35	22.125	20
	$NN1D_C$	11	28	17	16.5
ROI_C	$NN1M_C$	22	59	42.75	43
	$NN1D_C$	27	68	39.375	38

Qualitative analysis of the microscopic images depicted in Figure 15 yields unpsecific staining for $NN1M_C$ at 52 nM. Cells that do not express eGFP-gephyrin are stained by the peptide probe. Less unspicific staining is seen for $NN1D_C$ Figure 16. At 52 nM probe concentration, a cell with close to zero eGFP-expression shows close to zero staining by $NN1D_C$. Sensitivity is increased is increased compared to $NN1M_C$, as staining is visible at 0.07 nM probe concentration.

The qualitative analysis can be substantiated evaluation of all ROIs included in the dataset. At 1.92 nM probe concentration a median of 1.03 ($NN1D_C$) vs 0.05 ($NN1M_C$) integrated intensity can be recorded for ROI_B. Furthermore, specificity is increased for $NN1D_C$ compared to $NN1M_C$. At a concentration of 51.9, a linear relationship between the staining in the ROI_C (median 1.12) and ROI_B (median 1.06) can be observed (1.06 fold increase) for $NN1D_C$. In contrast, for $NN1M_C$ the median for ROI_C is 5.75 compared to a median of 0.72 for ROI_B (7.99 fold increase).

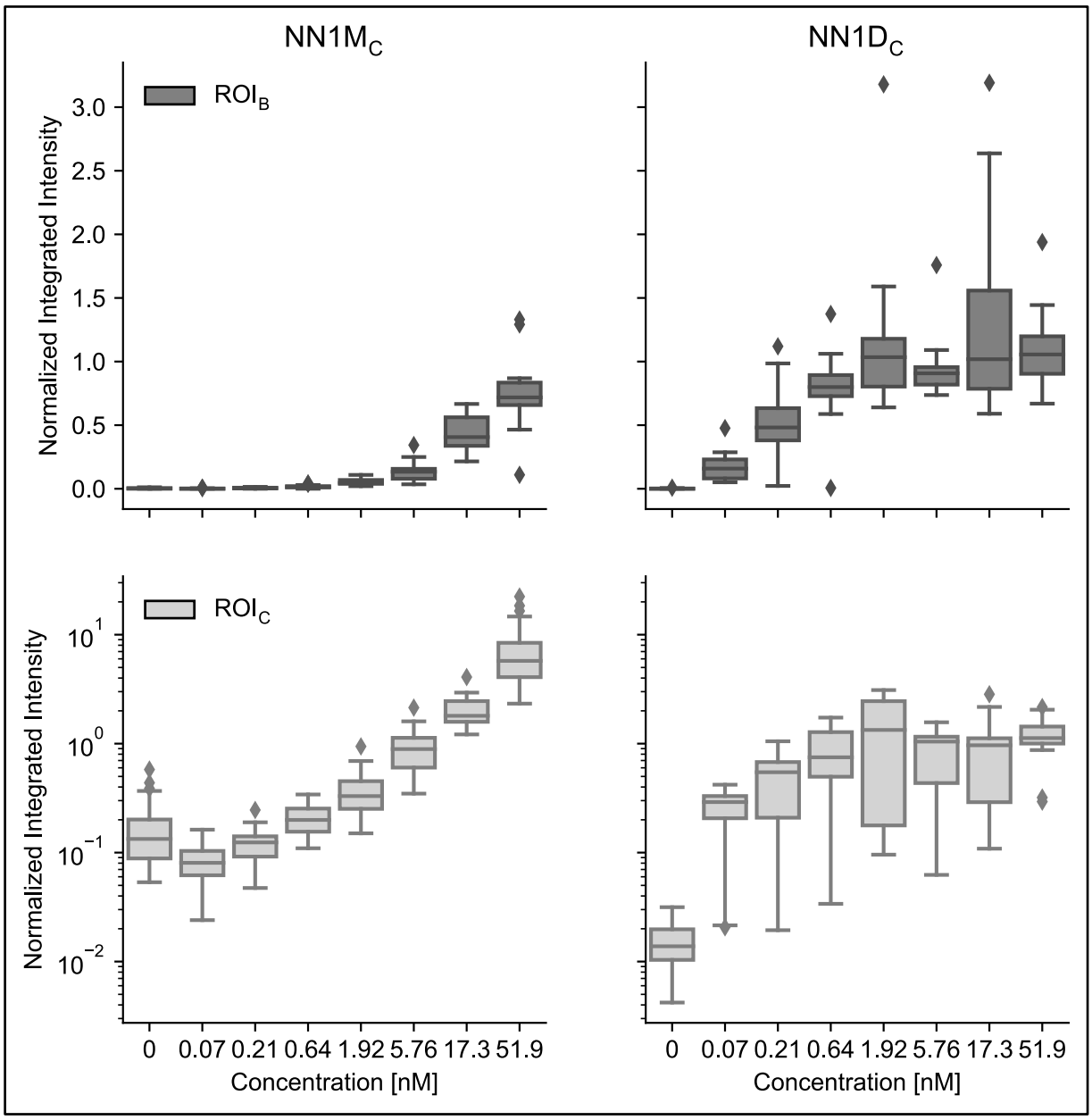

Figure 14 Boxplots showing normalized integrated intensity for different ROIs and compounds (MeOH fixation protocol). Columns represent the subgroup compounds (NN1M$_C$, NN1D$_C$), rows showing subgroup ROI (ROI$_B$, ROI$_C$). Of note: y-axis scale in linear scale (first row) and logarithmic scale (second row). NN1D$_C$ outperforms NN1M$_C$ in both specificity and sensitivity.

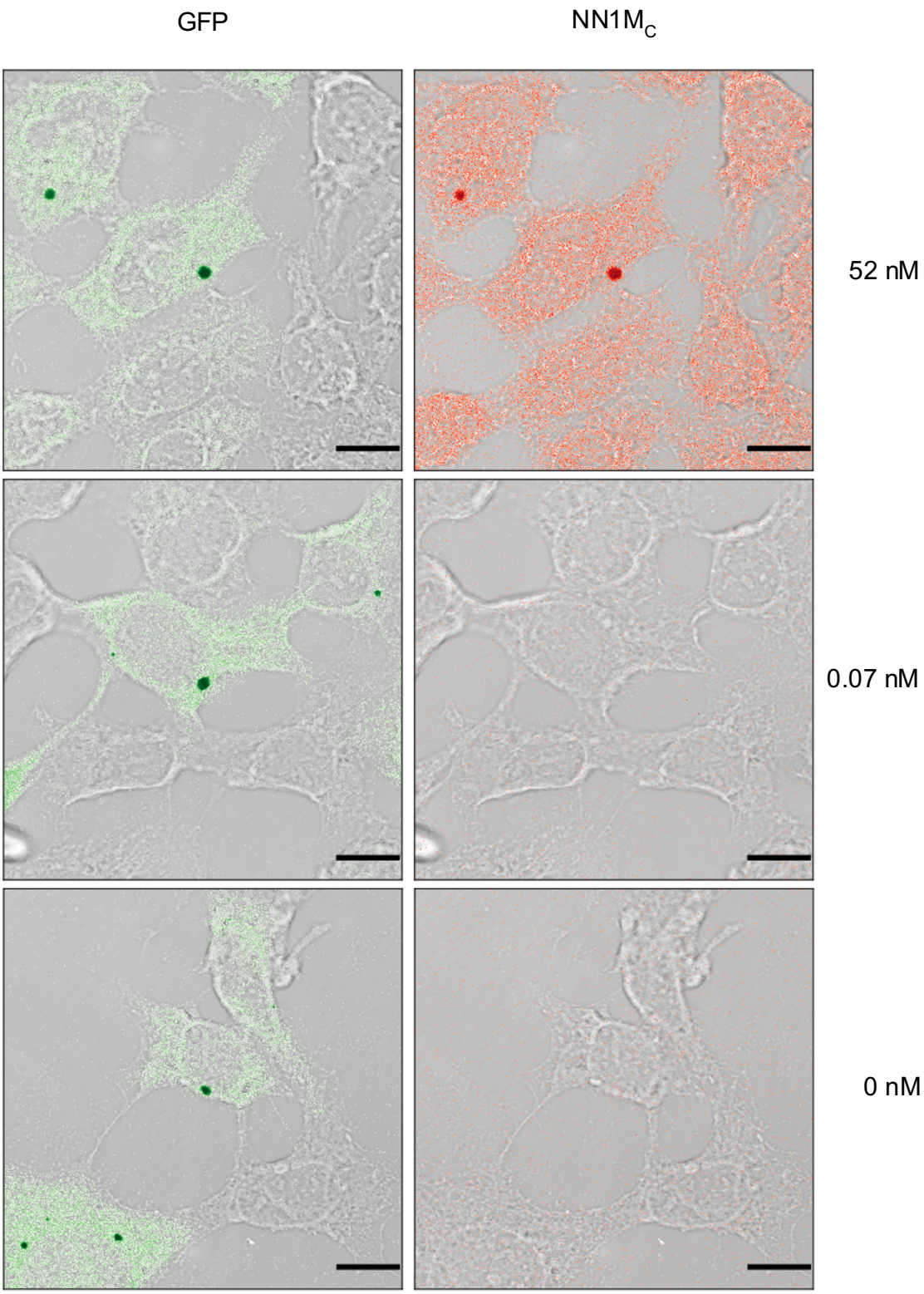

Figure 15 LSCM images of gephHEK fixed with MeOH and stained with NN1M$_c$ at different concentrations. eGFP channel is depicted on the left side, Cyanine5 channel on the right side. Images are presented as an overlay of the widefield and fluorescence channel. Concentration of NN1M$_c$ is indicated on the right. NN1M$_C$ shows unspecific staining at a concentration of 52 nM. Cells that do not express eGFP-gephyrin are stained. Scale bar = 15 µm.

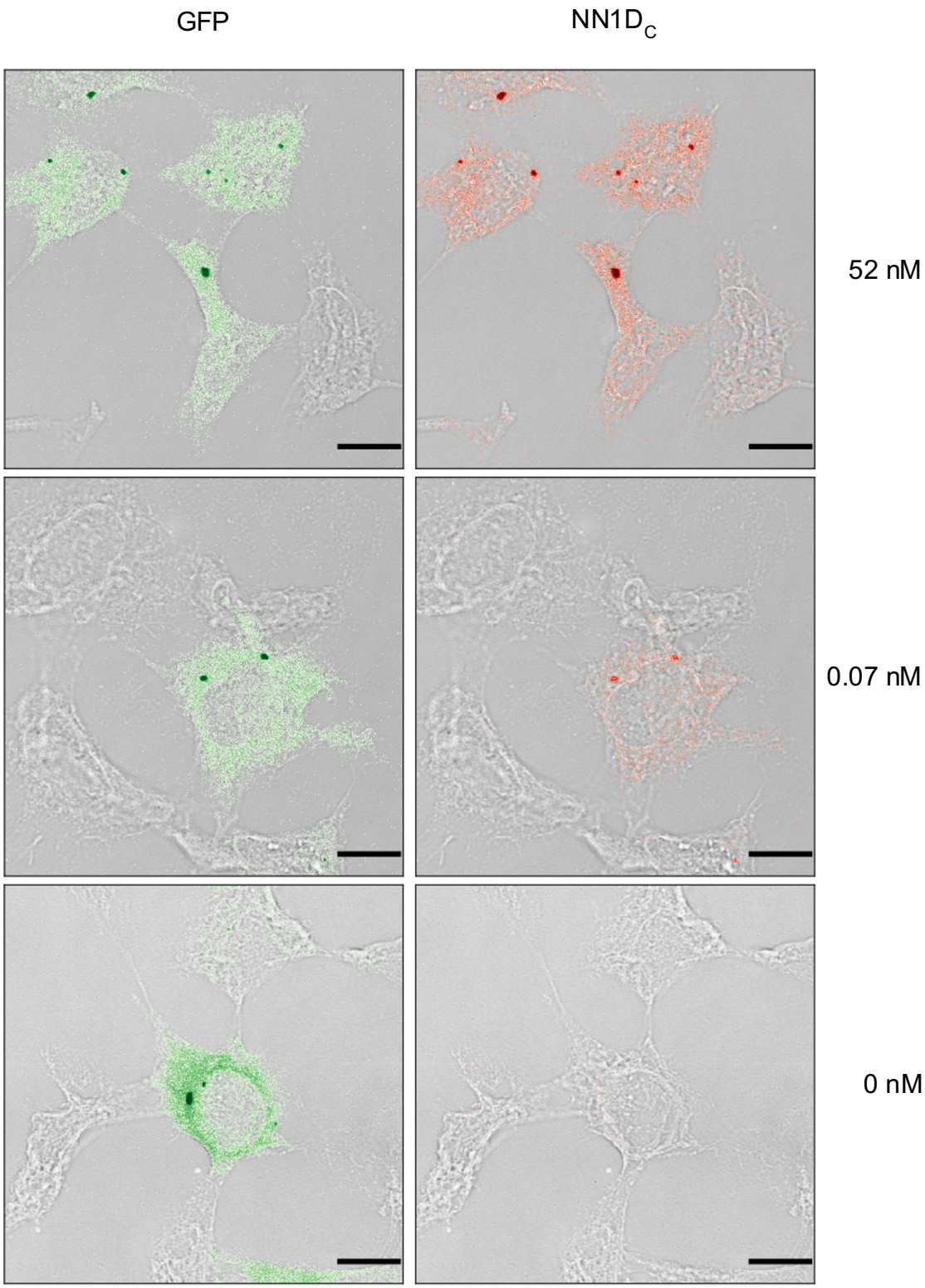

Figure 16 LSCM images of gephHEK fixed with MeOH and stained with NN1Dc at different concentrations. eGFP channel is depicted on the left side, Cyanine5 channel on the right side. Concentration of NN1D$_c$ is indicated on the right. eGFP-gephyrin is stained at a concentration of 0.07 nM NN1D$_C$ indicating high sensitivity. Scale bar = 15 µm.

4.13.2 Dose-response Relationship in gephHEK with Glyoxal Fixation

The experiment was repeated with different microscopy settings (HyD detector in photon counting mode) and glyoxal as a fixative (*see* Table 14**)**. Since MeOH is known to precipitate proteins and dehydrate cells, cell membrane structures are often damaged [55]. On the road towards the development of a fluorescent probe suitable for super resolution microscopy, glyoxal was chosen as a fixing agent due to its improved fixation properties compared to paraformaldehyde and MeOH [46]. The staining properties of $NN1D_C$ were compared to the monomeric peptide $_C$VK14 (Table 15). $_C$VK14 has the same binding sequence compared with $NN1D_C$. However, the fluorescent dye is located at the N-terminus via an NHS ester and a nona-L-arginine peptide is added at the C-terminus for better solvability and potential cell-penetration capabilities.

$NN1D_C$ was resynthesised (2.01 mg) in order to determine the concentration by weight. For both probes, a dilution series with the same concentrations as described earlier was prepared. GephHEK were fixed using the glyoxal fixation method (Table 14**)**. Mowiol containing 2.5% DABCO (1,4-diazabicyclo[2.2.2]octane) was used to reduce fading in fluorescent probes.

This time, 12-bit grayscale images (intensity values of 0-4095) were acquired with the Leica Hybrid Detector (HyD) in photon-counting mode in order to reduce saturated pixels and to obtain a quantifiable fluorescent signal. Gain was set to 10. Scan speed was set to 200 Hz. Image size was set to 1024x1024 pixels. The HCX PL APO lambda blue 63.0x1.40 OIL UV object with a numerical aperture of 1.4 was used for image acquisition. Excitation of GFP was achieved with 458 nm argon laser. Excitation of the peptide probe was achieved with 633 nm HeNe laser. HyD filter settings for GFP signal detection were set to 498-565 nm. sCy5 signal was detected at 653-695 nm. The intensity collected at each pixel is the sum of three images with the purpose of noise reduction. 5-7 images were acquired for every concentration at different sample locations. Images were automatically segmented as described earlier. Throughout the experiment microscopic settings were kept constant.

ROI_B with a pixel count of 15 and higher as well as ROI_C with a pixel count of 150 and higher were included in the analysis. ROIs, that had saturated pixels with a value of 4095 in the eGFP or Cyanine5 channel were excluded from the analysis. Descriptive statistics for ROI detection are presented in Table 18. Due to the altered microscopic settings no ROIs had to be excluded from analysis because of saturated pixels. This leads to a more homogeneous distribution of ROIs detected for each condition. For the negative control (0 nM concentration), a signal was detected in the sCy5 channel, most likely originating from bleed through of GFP signal.

Table 18 Number of ROIs for each concentration included in analysis for gephHEK with glyoxal as fixative. Descriptive statistics (min, max, mean, median) for number of ROIs detected.

ROI	Probe	min	max	mean	median
ROI_B	$_C$VK14	18	40	26.125	25
	$NN1D_C$	20	30	25	24
ROI_C	$_C$VK14	21	33	26.125	25
	$NN1D_C$	17	33	24.75	23

A high amount of unspecific staining is visible for $_C$VK14 at a concentration of 52 nM (*see* Figure 17) as $_C$VK14 seems to stain cells regardless of their eGFP-gephyrin expression levels. However, sensitivity for $_C$VK14 is high, as eGFP-gephyrin is stained at a concentration of 0.07 nM of the monomeric peptide probe. $NN1D_C$ shows less unspecific staining at a concentration of 52 nM, while still maintaining sensitivity at 0.07 nM (*see* Figure 18).

Figure 19 visualises the normalized intensity values for all conditions tested. A sigmoid dose-response relationship, especially for $NN1D_C$, can be assumed. This allows for fitting applying the four parameter logistic (4PL) regression [56], also known as Hill-equation. Fitting is shown in Figure 20. *scipy* (V1.7.3) was used for fitting [57].

Equation 8 4PL regression

$$y = d + \frac{a - d}{1 + (\frac{x}{c})^b}$$

a = y value of asymptote at min concentration
b = slope factor
c = point of inflection (EC_{50})
d = y value of asymptote at max concentration
y = response

Whilst the EC_{50} value for $NN1D_c$ is in the same order of magnitude for both ROIs, $_c$VK14 shows a higher EC_{50} value for ROI_C (8764.83) when compared to ROI_B (7.45). This indicates more specific staining of eGFP-gephyrin in GephHEK for $NN1D_c$ when compared to $_c$VK14.

Lower EC_{50} values of for both ROIs for $NN1D_C$ indicate higher sensitivity when compared to $_C$VK14.

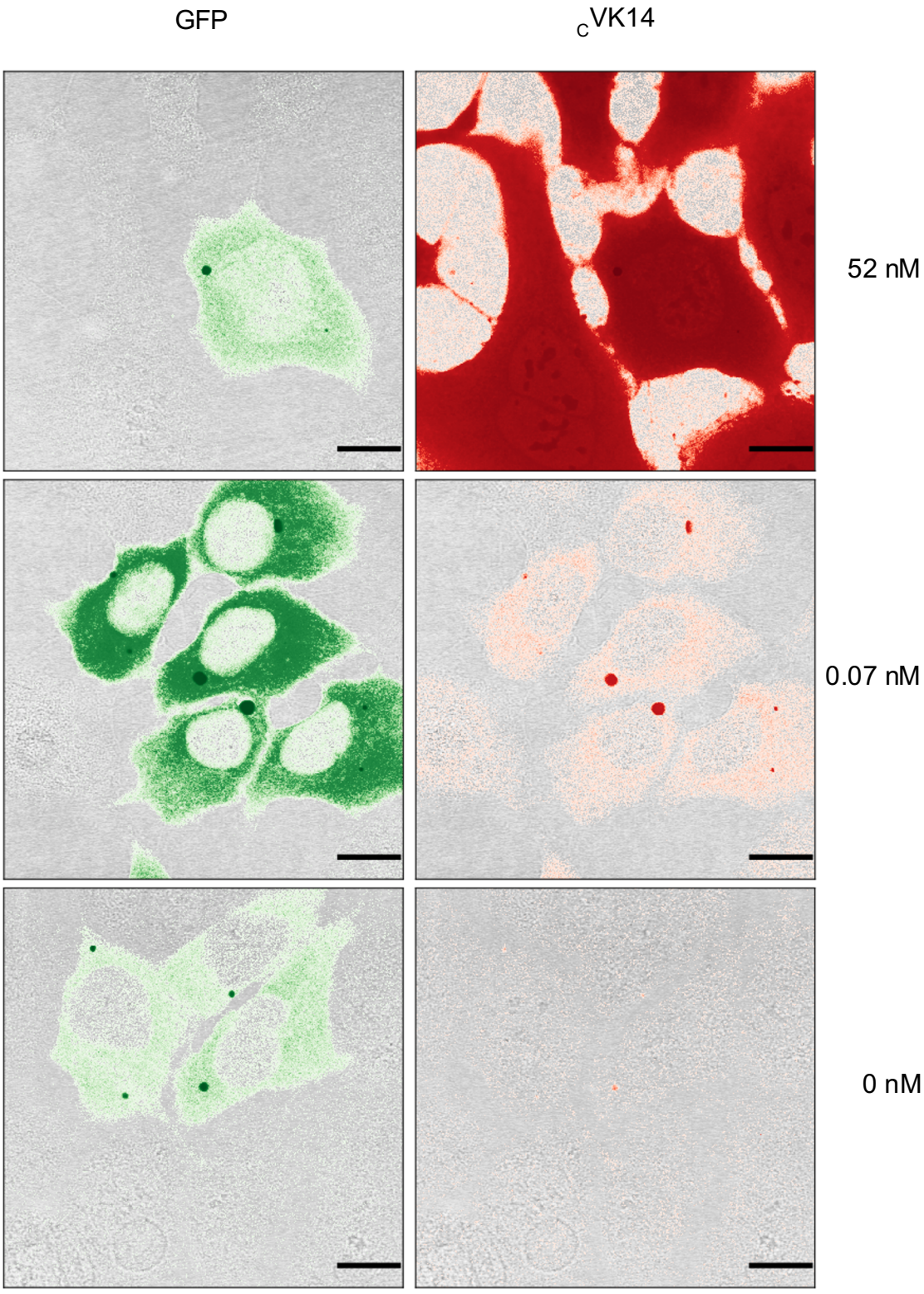

Figure 17 LSCM images of gephHEK fixed with glyoxal and stained with $_{c}$VK14 at different concentrations. eGFP channel is depicted on the left side, Cyanine5 channel on the right side. Scale bar = 15 µm.

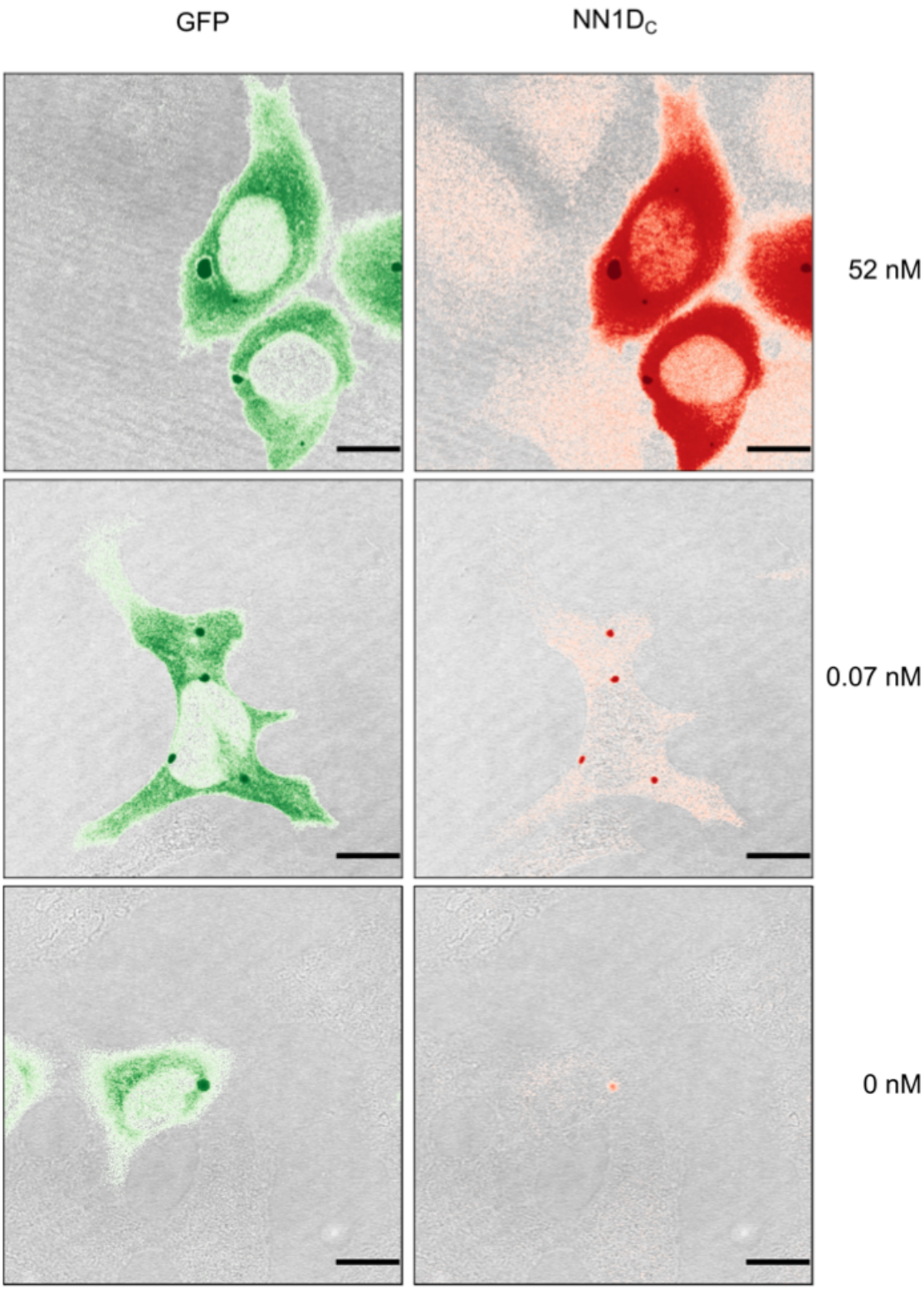

Figure 18 LSCM images of gephHEK fixed with glyoxal and stained with NN1D$_c$ at different concentrations. eGFP channel is depicted on the left side, sCy5 channel on the right side. Scale bar = 15 μm.

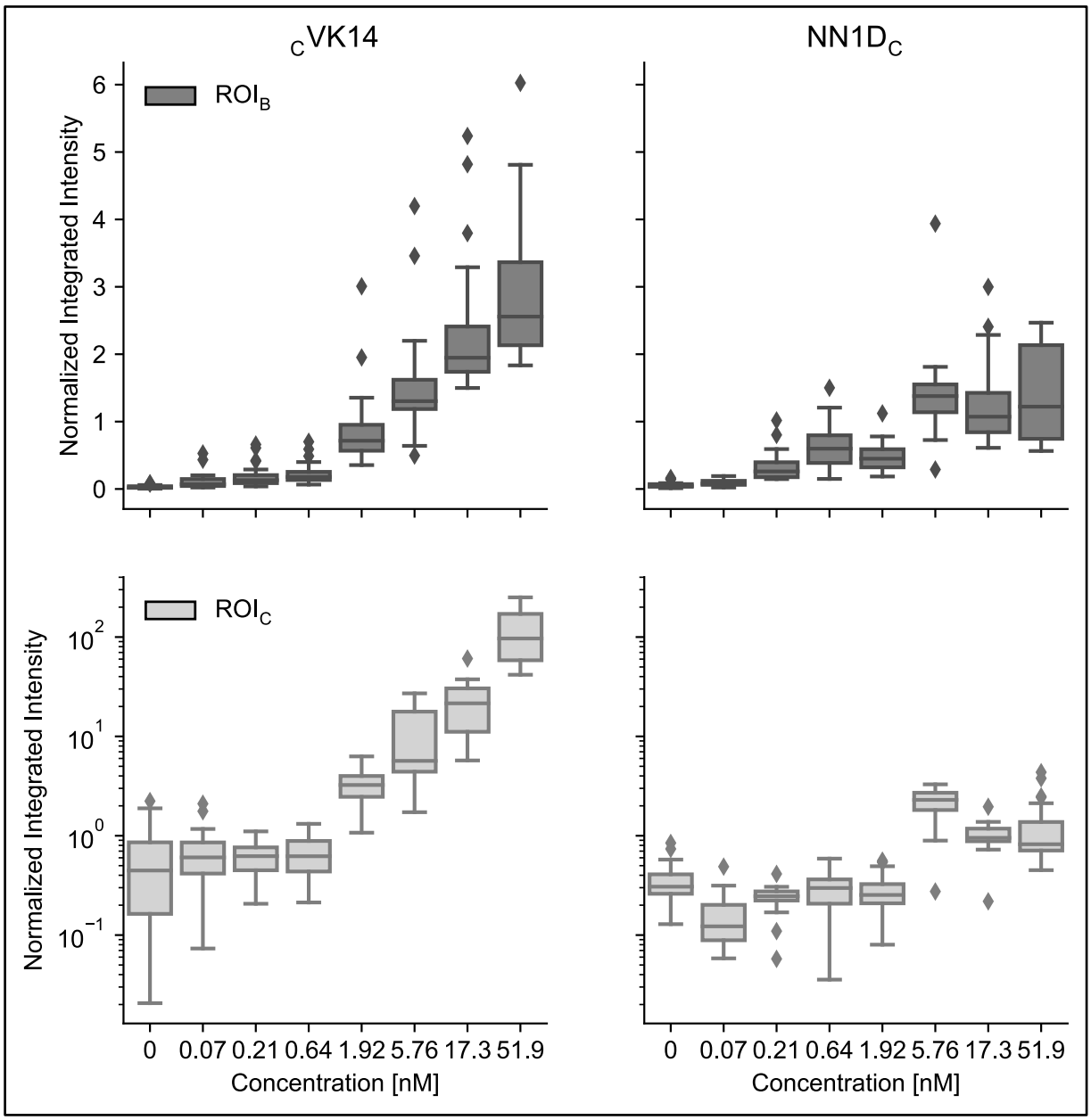

Figure 19 Boxplots showing normalized integrated intensity for different ROIs and compounds (glyoxal fixation protocol). Columns represent different compounds ($_C$VK14, NN1D$_C$), rows show different ROIs (ROI$_B$; ROI$_C$). Of note: y-axis in linear scale (first row, ROI$_B$) and logarithmic scale (second row, ROI$_C$). For fitting of the dose response curves refer to Figure 20.

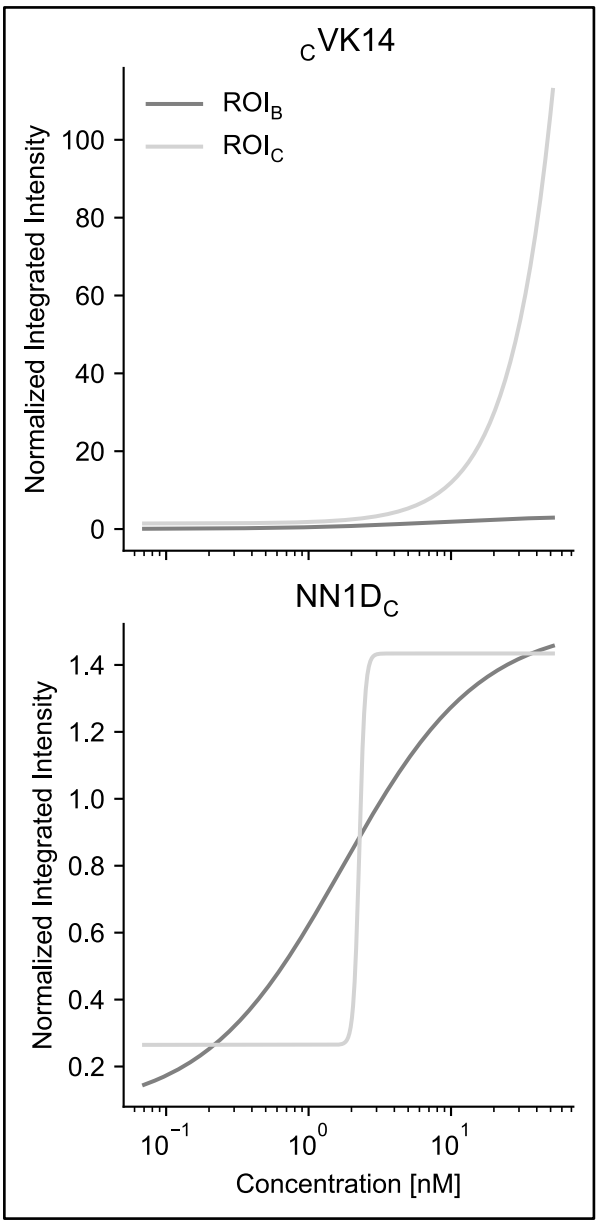

Probe	Region	EC_{50} [nM]
$_C$VK14	ROI$_B$	7.45
$_C$VK14	ROI$_C$	8764.83
NN1D$_C$	ROI$_B$	1.72
NN1D$_C$	ROI$_C$	2.27

Figure 20 Applied at low nanomolar concentrations NN1D$_C$ but not $_C$VK14 visualises gephyrin with high sensitivity and specificity. Dose-Response-Curve (4PL) fitting for normalized integrated intensity values of different compounds (row) and ROIs (colour) on the left for glyoxale fixation. Be aware of different range for y-scale for the different compounds.
The overlapping dose-response curves for NN1D$_C$ indicate a close to linear relationship between normalized integrated intensity for different ROIs indicating specific staining.
Table above lists metrics for curve fitting. Differences of EC_{50} values for NN1D$_C$ for different ROIs are lower as for $_C$VK14 indicating more specific staining of eGFP-gephyrin. Refer to Supplementary Table 1 for more detailed metrics.

4.13.3 Limitations of the Study

It could be shown that the main staining properties like sensitivity and specificity for gephHEK cells could be improved by applying the dimeric probe NN1D$_C$. However, a couple assumptions were necessary for data evaluation.

First, it was assumed that gephHEK do not, or at least only to a negligible degree, express native gephyrin, which is supported by the fact that the GEPH-gene is encoded in chromosome 14 in HEK293 cells [58]. This would lead to a higher background measured for all probes tested. A higher background would affect the normalised integrated intensity of ROI$_c$ to higher extend compared ROI$_B$ because of lower signal. However, probes would remain comparable to each other, because this signal would be added to all probes collectively.

Second, the assumption was made, that staining of eGFP of the peptide probe is linear for both cellular ROIs. However, ROI_B yields a higher eGFP signal due to a concentration increase of GFP-gephryin. This could lead to a higher likeliness of ROI_B being stained compared to ROI_C due to the concept of functional affinity described earlier. However, in our case this theoretic effect could not be observed, most likely because of unspecific binding of the probe to ROI_C. In order to address this concern experimentally, a control assay was performed presented in the following subsection.
Third, excitation and emission spectra of the fluorescent dye could have change due to conjugation of different probes. Thus, fluorescence spectroscopy was performed.

4.13.4 Fluorescence Spectroscopy

Probes tested above were diluted to a concentration of 3.3 µM in PBS. Excitation and emission spectra were recorded in FluoroMax4. For measurements of the emission spectrum, excitation was performed with the excitation xenon-lamp at 610 nm. Front entrance and exit slit were set to 2 nm bandpass. Emission was subsequentially recorded [620 nm – 800 nm] at an increment of 1 nm with a front entrance and exit slit of 1 nm. Corrected signal (S1c/R1) was recorded.
For measurements of the excitation spectrum, excitation was performed using the excitation xenon-lamp. Bandpass filter with a front entrance and exit slit of 1 nm was incremented 1 nm per measurement [500 nm – 660 nm]. Excitation spectrum was recorded at 670 nm, entrance and exit slit were set to 0.5 nm.
Spectra were internally normalised. As shown in Figure 21, emission and excitation spectra were comparable to each other in shape. Unconjugated sCy5 had the lowest maxima with a wavelength of ex_{max} = 645 nm and em_{max} = 662 nm. $NN1D_C$ had peaks at a wavelength of ex_{max} = 649 nm and em_{max} = 667 nm.

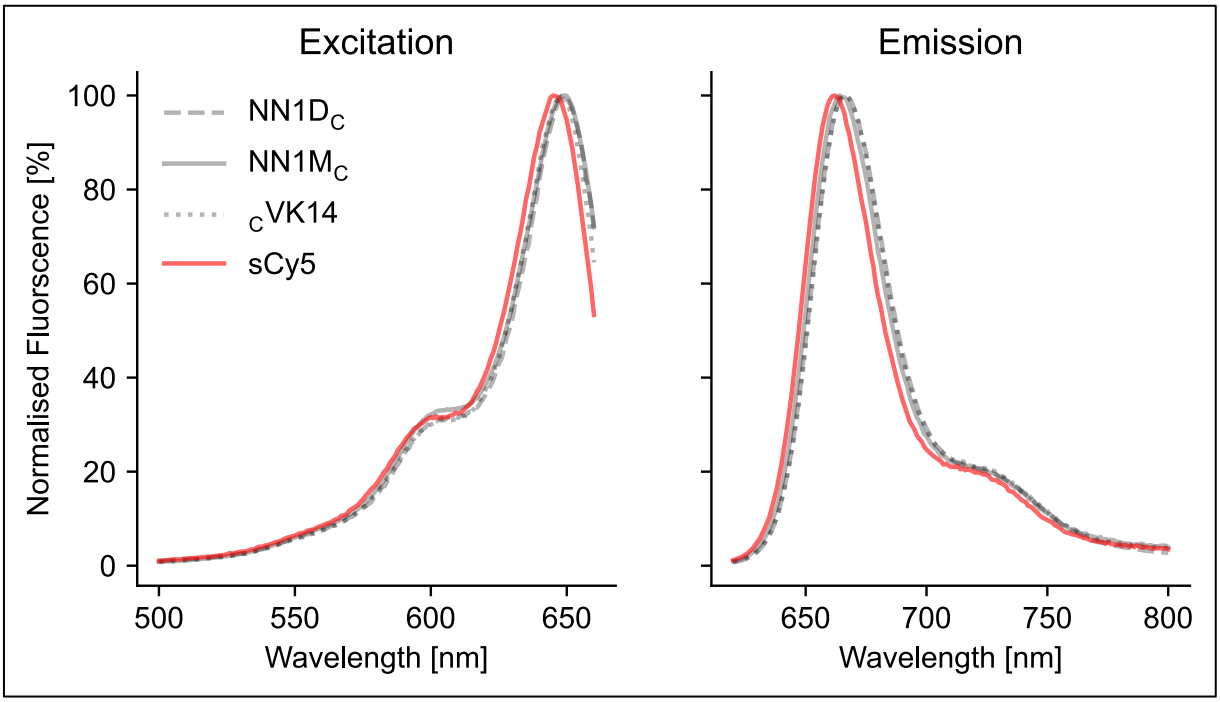

Figure 21 Fluorescence spectrum for probes synthesised. Peptide probes (NN1D$_C$, NN1M$_C$, $_c$VK14) overlapping, indication similar fluorescence spectra.

4.13.5 HEK293-WT Staining

In order to address the second concern described earlier, HEK293-WT cells were cultivated as described in 3.5.1 and fixed with MeOH. Immunolabelled with 3B11 mouse monoclonal antibody (1st, D=1000, µL) and goat anti-mouse IgG secondary antibody, Alexa Fluor 555 (2nd, D=2000, µL) was performed as described in subsection 3.6.1.

LSCM was performed. 8-bit grayscale images (intensity values of 0-255) were acquired with the Leica Hybrid Detector (HyD) in photon multiplier mode for greatest sensitivity. Gain was set to 214. Scan speed was set to 100 Hz. Image size was set to 1024x1024 pixels. The HCX PL APO lambda blue 63.0x1.40 OIL UV object with a numerical aperture of 1.4 was used for image acquisition. Excitation of GFP was achieved with 458 nm argon laser. Excitation of the peptide probe was achieved with 561 nm DPSS laser. HyD filter settings for GFP signal detection were set to 506-537 nm. Alexa Fluor 555 signal was detected at 603-672 nm. Throughout the experiment microscopic settings were kept constant. eGFP and Alexa Fluor 555 signal intensities were analysed in a qualitative manner.

As presented in Figure 22 there was no staining present in the HEK293 WT, whilst the positive control gephHEK was stained. This indicates that background resulting from endogenous gephyrin expression in HEK293 can be neglectable.

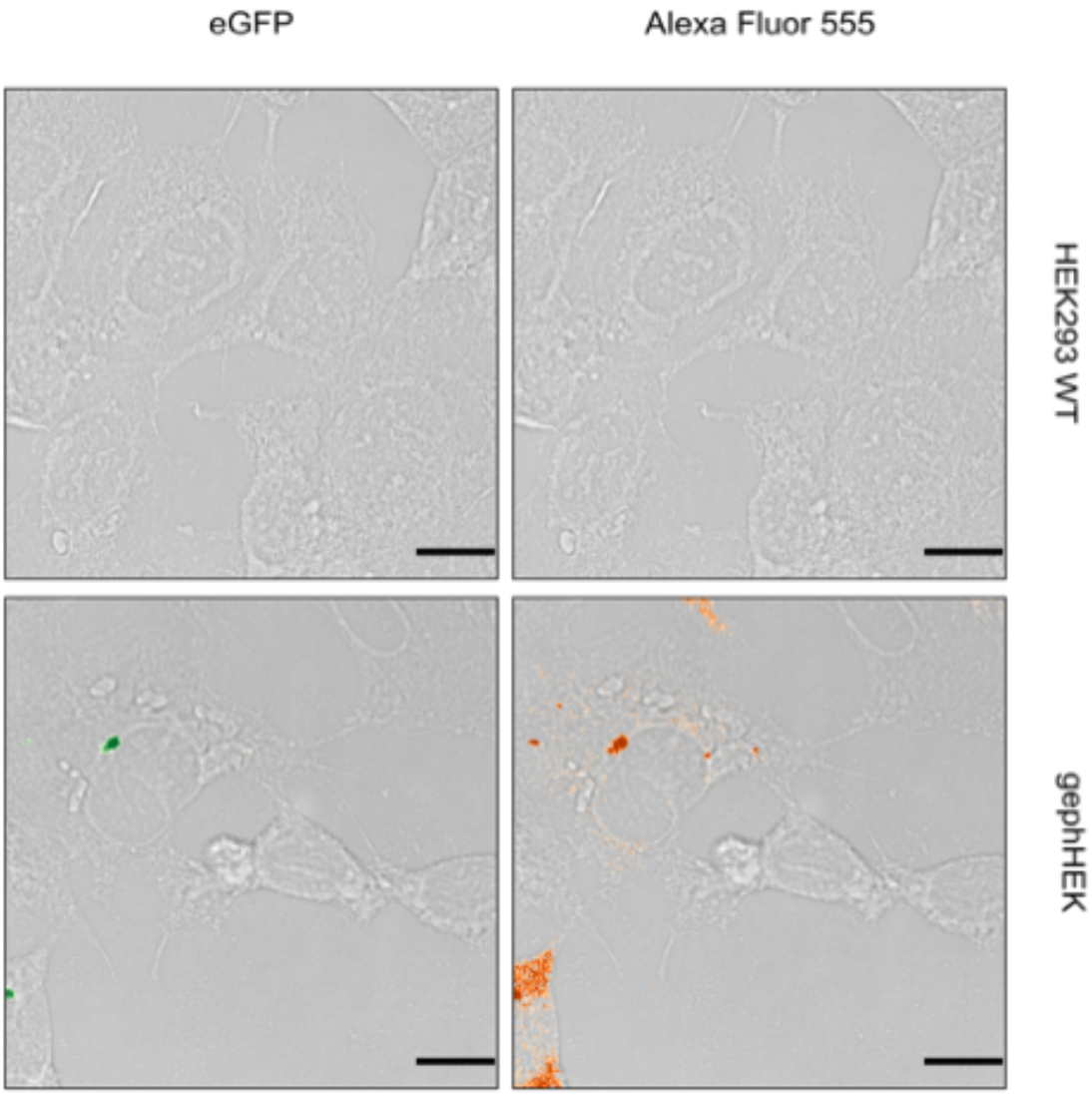

Figure 22 HEK293 WT cells express no significant amount of endogenous gephyrin. Thus, background signal from endogenous gephyrin in gephHEK can be assumed to be negligible. First row shows HEK293 WT staining with anti-gephyrin 3B11 antibody and anti-mouse IgG antibody. Second row shows staining of gephHEK as positive control for staining protocol.

4.14 Fixation Methods

Throughout this thesis multiple fixation methods have been used. While MeOH permeates and fixes cells via dehydration and protein precipitation, the cell membrane and cytoplasmic structures are damaged [59]. Furthermore, it was reported, that ≤ 20% of the POIs can still be clustered by antibodies or multivalent probes after fixation [60]. On top, MeOH as a fixative can lead to the complete loss of eGFP signal intensity in transiently transfected free GFP expressing Chinese hamster ovary cells [61]. In our case, the eGFP signal intensity correlated with the probe's signal intensity tested.

However, if PPIs are subject of investigation, other fixation methods like aldehyde fixation can more appropriate. Aldehydes like glyoxal or formaldehyde crosslink proteins which can lead

to decreased immunoreactivity during immunostaining due to masked epitopes as depicted in Figure 23 [59, 62, 63]. In our case, gephHEK could be fixed with either MeOH, paraformaldehyde or glyoxal, while still maintaining eGFP signal and allowing labelling with the functional peptide probes (Figure 24).

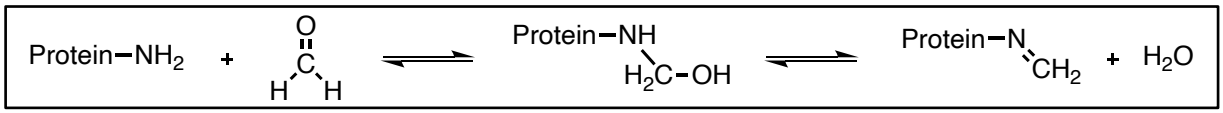

Figure 23 Formation of Schiff-Base during formaldehyde crosslinking of biomolecules. In a first step, formaldehyde reacts with a strong nucleophile like the primary amine of the lysine side chain. Next, a methylol intermediate is formed that can yield an imine (Schiff-Base). In a second step the imine can than react with nucleophilic residues like N-terminal amino groups and side chains of cysteine, histidine, lysine, tryptophan arginine or an amino group of a DNA base [56].

In 2018, Richter et al. found, that glyoxal would induce less morphological changes to the specimen during fixation and is superior in terms of rapid tissue penetration and stronger cross-linking of proteins while maintaining immunoreactivity for most samples [64]. Therefore, we choose glyoxal fixation as the fixation method for further experiments.

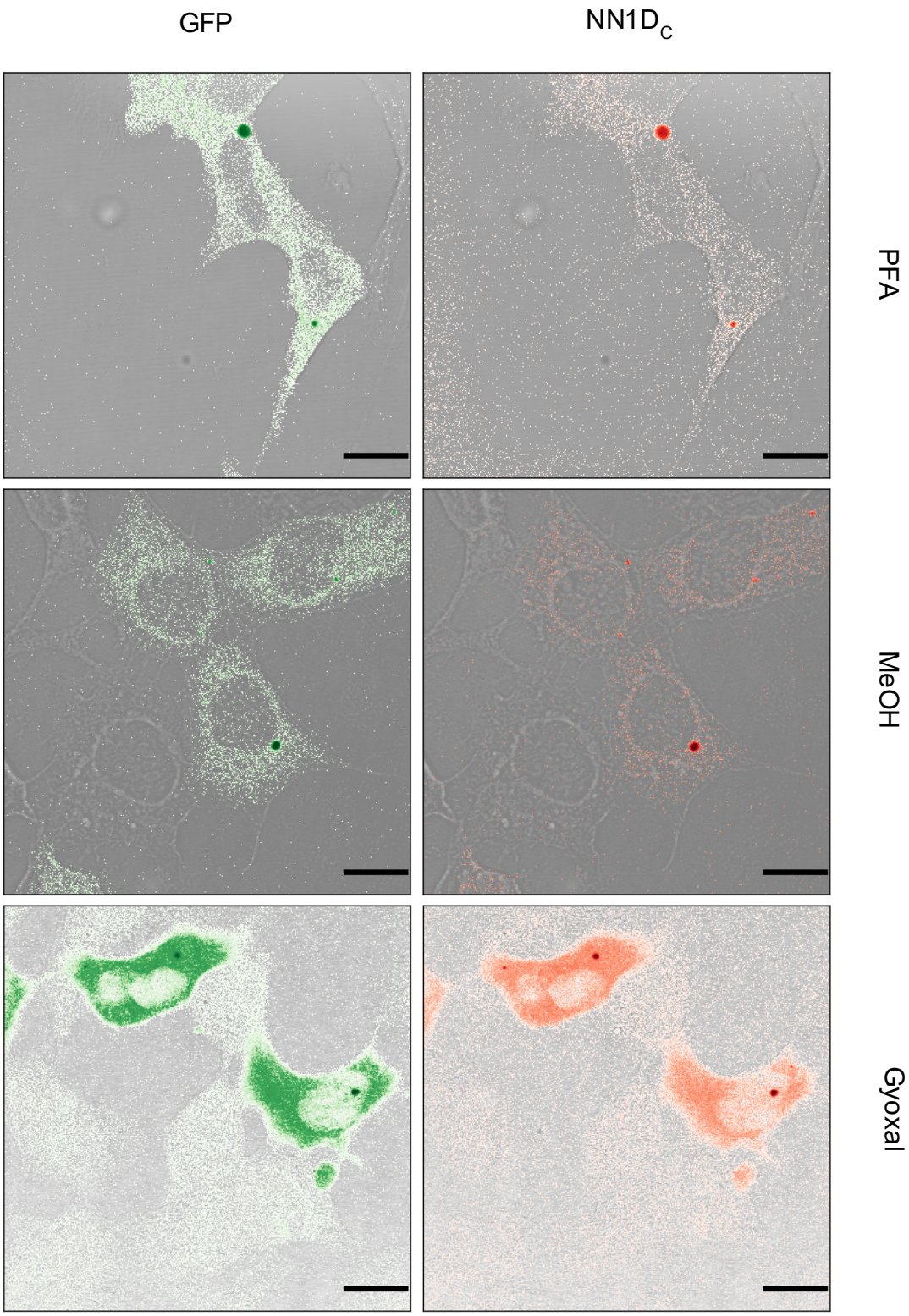

Figure 24 Peptide probe staining (NN1D$_C$) of gephHEK cells with different fixation protocols. Images represent an overlay of the brightfield channel with the filter settings for eGFP (left) and the peptide probe (right) in the Cyanine 5 filter. All fixation methods applied yield a signal in the eGFP channel and allow for staining with dimeric peptide probes. Images have been acquired using different microscopic settings and are thus not comparable in terms of staining intensities. Scale bar = 15 µm.

5 Summary and Outlook

My here presented work contributed critically to the development of a highly sensitive and highly specific dimeric fluorescent gephyrin probe and its application for high-throughput affinity measurements and visualization of the inhibitory synapse. This is substantiated by recent co-authorships [50, 65]. The provided data established $NN1D_C$ as a high contrast probe for cellular imaging when applied at low nanomolar concentrations.

5.1 Use as Versatile Probe for Synapse Imaging

In contrast to antibodies which are raised against protein fragments that generally do not relate to a specific protein function, the here studied peptide-based probes are derived from the GlyR, an endogenous ligand of neuronal gephyrin. The resulting probes were found to bind exclusively gephyrin isoforms that actively cluster receptors at the synapse. The introduced cysteine containing linker proved useful for flexible conjugation of different maleimide containing dyes and other maleimide containing functional groups. This enabled a straightforward derivatization of the binder to yield a fluorescent probe with imaging capabilities. Thus, the binding hierarchy of a multivalent peptide probe followed by a monovalent binding peptide probe could be translated to LSCM.
Furthermore, the immunostainings following my initial experiments show several advantages over the large sized conventional immunostainings with antibodies [65]. The improved linearity of binding within the optimal concentration range as highlighted in the here presented data analysis enabled eventually quantification of the target protein in neurons [65]. An additional feature that was explored following my initial works was the application on tissues. Here an enhanced penetration motive compared to conventional antibody staining was observed [65].

The established image segmentation and analysis pipeline improved data quality and reproducibility of the results provided. It is highly customisable, fast and written in pure python, making it possible for researchers to further expand and modify segmentation properties based on their needs.

5.2 Future Application for Live Imaging

The probes synthesized in this work are only applied in fixed cells because these probes do not allow for the passage of the cell membrane independently due to their size, charge, and hydrophilic nature. Cellular uptake could be made possible by further functionalization of the peptide through conjugation with a cell-penetrating peptide. For this purpose, the peptide could be enabled to harbour free thiol groups, which would allow for reversible conjugation of

cell-penetrating peptides through disulfide bonds. Namely TAT or pol-arg motives could be added for membrane permeability. These highly cationic cell-penetrating peptides bind to the cell membrane to enhance endocytosis [66].

Further derivatives of the peptide probe can be synthesized by exchanging the fluorescent signalling agent with other signalling agents such as radioactive nucleotides that would allow for methods such single-photon emission computed tomography (SPECT).

5.3 Use for High-throughput Screening of Gephyrin

High-throughput screening of gephyrin required to overcome the inherent caveats of currently used binding read-outs. Array-based techniques for example suffer from immobilization-related artifacts resulting from peptide inactivation or unspecific accumulation of gephyrin depending on orientation, surface chemistry, and ligand density. Here my probe turned out useful to screen binding in solution using temperature related intensity change (TRIC). Compared with conventional MST setups, TRIC allows for even smaller sample volumes and is compatible with microtiter plates and thus facilitates higher throughput and automatization [13].

Large libraries of unmodified ligands are often analysed with fluorescently labelled proteins. Here, Alexa 647-labeled gephE exhibited unspecific peptide binding (Figure S1A, Schulte, 2021) as commonly observed. Among the tested alternative labelling strategies, Red-Maleimide second generation. (Nanotemper Technologies GmbH)-labelled gephE performed best (Figure 2A, *ibid*). Yet, the observed low signal amplitude required the development of alternative approaches for sensitive and effective screening. To this end, a displacement assay was set-up on which a variant of my fluorescently labelled tracer was used to generate an enhanced TRIC response [50]. Displacement of this binder yields an inverse TRIC signal and enables the robust affinity determination of soluble gephyrin binders [50] and highlights how similar probes could be exploited for enable the screening of other target proteins. Notably, due to the dimeric nature and the resulting high affinity $NN1D_C$ provided a large dynamic range for TRIC measurements, even when applied at nanomolar concentrations.

TRIC measurements in combination with the displacement assay described earlier could also be beneficial for the screening of other therapeutic molecules targeting gephE. Thus, the proposed method could function as a hub for further fragment-based drug development of a small molecule. Artemisinins, a group of small molecules primarily used for treatment of malaria, could already be shown to bind gephE [67]. This method could be applied to develop new small molecules with increased affinity based on artemisinin. One way of achieving higher affinity could be by dimerising artemisinin using hydrophilic peg-linkers of different size in order to increase solubility.

6 Annotations

1. *The Nobel Prize in Chemistry*. 2014 [cited 25.05.2022]; Available from: https://www.nobelprize.org/prizes/chemistry/2014/prize-announcement/.
2. Weisenburger, S. and V. Sandoghdar, *Light microscopy: an ongoing contemporary revolution*, in *Contemporary Physics*. 2015, Informa UK Limited. p. 123-143.
3. Valeur, B. and M.N. Berberan-Santos, *A Brief History of Fluorescence and Phosphorescence before the Emergence of Quantum Theory*, in *Journal of Chemical Education*. 2011, American Chemical Society (ACS). p. 731-738.
4. Klein, T., S. Proppert, and M. Sauer, *Eight years of single-molecule localization microscopy*, in *Histochemistry and Cell Biology*. 2014, Springer Science and Business Media LLC. p. 561-575.
5. Heintzmann, R. and G. Ficz, *Breaking the Resolution Limit in Light Microscopy.* Digital Microscopy, 2013: p. 525-544.
6. *The Nobel Prize in Chemistry*. 2008 [cited 04.04.2022]; Available from: https://www.nobelprize.org/prizes/chemistry/2008/press-release/.
7. Day, R.N. and M.W. Davidson, *The fluorescent protein palette: tools for cellular imaging*, in *Chemical Society Reviews*. 2009, Royal Society of Chemistry (RSC). p. 2887.
8. Ganini, D., et al., *Fluorescent proteins such as eGFP lead to catalytic oxidative stress in cells*, in *Redox Biology*. 2017, Elsevier BV. p. 462-468.
9. Ansari, A.M., et al., *Cellular GFP Toxicity and Immunogenicity: Potential Confounders in in Vivo Cell Tracking Experiments*, in *Stem Cell Reviews and Reports*. 2016, Springer Nature. p. 553-559.
10. Saal, K.-A., et al., *Combined Use of Unnatural Amino Acids Enables Dual-Color Super-Resolution Imaging of Proteins via Click Chemistry*, in *ACS Nano*. 2018, American Chemical Society (ACS). p. 12247-12254.
11. Beliu, G., et al., *Bioorthogonal labeling with tetrazine-dyes for super-resolution microscopy*, in *Communications Biology*. 2019, Springer Science and Business Media LLC.
12. Hughes, L.D., R.J. Rawle, and S.G. Boxer, *Choose Your Label Wisely: Water-Soluble Fluorophores Often Interact with Lipid Bilayers.* PLoS ONE, 2014.
13. Gupta, A.J., S. Duhr, and P. Baaske, *Microscale Thermophoresis (MST)*, in *Encyclopedia of Biophysics*, G. Roberts and A. Watts, Editors. 2018, Springer Berlin Heidelberg: Berlin, Heidelberg. p. 1-5.
14. Wienken, C.J., et al., *Protein-binding assays in biological liquids using microscale thermophoresis*, in *Nature Communications*. 2010, Springer Science and Business Media LLC.
15. Greving, M.P., et al., *High-throughput screening in two dimensions: Binding intensity and off-rate on a peptide microarray*, in *Analytical Biochemistry*. 2010, Elsevier BV. p. 93-95.
16. Volkmer, R., V. Tapia, and C. Landgraf, *Synthetic peptide arrays for investigating protein interaction domains*, in *FEBS Letters*. 2012, Wiley. p. 2780-2786.
17. Vauquelin, G. and S.J. Charlton, *Exploring avidity: understanding the potential gains in functional affinity and target residence time of bivalent and heterobivalent ligands*, in *British Journal of Pharmacology*. 2013, Wiley. p. 1771-1785.
18. A. H. Coons, et al., *The Demonstration of Pneumococcal Antigen in Tissues by the Use of Fluorescent Antibody.* The Journal of Immunology, 1942.
19. Vira, S., et al., *Fluorescent-labeled antibodies: Balancing functionality and degree of labeling.* Analytical Biochemistry, 2010: p. 146-150.
20. Maidorn, M., S.O. Rizzoli, and F. Opazo, *Tools and limitations to study the molecular composition of synapses by fluorescence microscopy.* Biochemical Journal, 2016: p. 3385-3399.

21. Schermelleh, L., R. Heintzmann, and H. Leonhardt, *A guide to super-resolution fluorescence microscopy.* J Cell Biol, 2010: p. 165-175.
22. van de Linde, S., et al., *Direct stochastic optical reconstruction microscopy with standard fluorescent probes.* Nature Protocols, 2011: p. 991-1009.
23. Ries, J., et al., *A simple, versatile method for GFP-based super-resolution microscopy via nanobodies.* Nat Methods, 2012: p. 582-584.
24. Beghein, E. and J. Gettemans, *Nanobody Technology: A Versatile Toolkit for Microscopic Imaging, Protein--Protein Interaction Analysis, and Protein Function Exploration.* Frontiers in Immunology, 2017.
25. Dong, J.-X., et al., *A toolbox of nanobodies developed and validated for use as intrabodies and nanoscale immunolabels in mammalian brain neurons.* eLife, 2019.
26. Staderini, M., et al., *Peptides for optical medical imaging and steps towards therapy.* Bioorganic & Medicinal Chemistry, 2018: p. 2816-2826.
27. *Drugs@FDA: FDA-Approved Drugs*. 2021 [cited 25.05.2022]; Available from: https://www.accessdata.fda.gov/scripts/cder/daf/index.cfm?event=overview.process&ApplNo=020314.
28. Lee, S., J. Xie, and X. Chen, *Peptide-Based Probes for Targeted Molecular Imaging.* Biochemistry, 2010: p. 1364-1376.
29. Lukinavičius, G., et al., *Fluorogenic probes for live-cell imaging of the cytoskeleton.* Nature Methods, 2014: p. 731-733.
30. Maric, H.M., et al., *Gephyrin-binding peptides visualize postsynaptic sites and modulate neurotransmission.* Nature Chemical Biology, 2016: p. 153.
31. Deetjen, P., E.J. Speckmann, and J. Hescheler, *Physiologie*. 2005: Elsevier GmbH, Urban & Fischer Verlag.
32. Specht, C.G., *Fractional occupancy of synaptic binding sites and the molecular plasticity of inhibitory synapses.* Neuropharmacology, 2020. **169**: p. 107493.
33. Kim, E.Y., et al., *Deciphering the structural framework of glycine receptor anchoring by gephyrin.* The EMBO Journal, 2006: p. 1385-1395.
34. Sola, M., et al., *X-ray Crystal Structure of the Trimeric N-terminal Domain of Gephyrin.* Journal of Biological Chemistry, 2001: p. 25294-25301.
35. Groeneweg, F.L., et al., *Gephyrin: a key regulatory protein of inhibitory synapses and beyond.* Histochem Cell Biol, 2018: p. 489-508.
36. Maric, H.-M., et al., *Gephyrin-mediated γ-aminobutyric acid type A and glycine receptor clustering relies on a common binding site.* The Journal of biological chemistry, 2011: p. 42105-42114.
37. Uezu, A., et al., *Identification of an elaborate complex mediating postsynaptic inhibition.* Science, 2016: p. 1123-1129.
38. Dos Reis, R., et al., *Complex regulation of Gephyrin splicing is a determinant of inhibitory postsynaptic diversity.* Nature Communications, 2022. **13**(1): p. 3507.
39. Essrich, C., et al., *Postsynaptic clustering of major GABAA receptor subtypes requires the gamma 2 subunit and gephyrin.* Nature Neuroscience, 1998: p. 563-571.
40. Specht, C.G., et al., *Quantitative Nanoscopy of Inhibitory Synapses: Counting Gephyrin Molecules and Receptor Binding Sites.* Neuron, 2013: p. 308-321.
41. Jaradat, D.M.M., *Thirteen decades of peptide synthesis: key developments in solid phase peptide synthesis and amide bond formation utilized in peptide ligation*, in *Amino Acids*. 2017, Springer Science and Business Media LLC. p. 39-68.
42. Palomo, J.M., *Solid-phase peptide synthesis: an overview focused on the preparation of biologically relevant peptides.* 2014: p. 32658-32672.
43. Eissler, S., et al., *Substitution determination of Fmoc-substituted resins at different wavelengths.* J Pept Sci, 2017: p. 757-762.
44. Prior, P., et al., *Primary structure and alternative splice variants of gephyrin, a putative glycine receptor-tubulin linker protein.* Neuron, 1992. **8**(6): p. 1161-70.
45. Fuhrmann, J.C., et al., *Gephyrin Interacts with Dynein Light Chains 1 and 2, Components of Motor Protein Complexes*, in *The Journal of Neuroscience*. 2002, Society for Neuroscience. p. 5393-5402.

46. Richter, K.N., et al., *Glyoxal as an alternative fixative to formaldehyde in immunostaining and super-resolution microscopy.*, in *EMBO J*. 2018: Department of Neuro- and Sensory Physiology, University of Göttingen Medical Center, Göttingen, Germany.; Cluster of Excellence Nanoscale Microscopy and Molecular Physiology of the Brain, Göttingen, Germany.; Department of Neuro- and Sensory Physiology, U. p. 139-159.
47. Johnson, J., *Not seeing is not believing: improving the visibility of your fluorescence images*, in *Molecular Biology of the Cell*, D. Kellogg, Editor. 2012, American Society for Cell Biology (ASCB). p. 754-757.
48. Maric, H.M., V.B. Kasaragod, and H. Schindelin, *Modulation of Gephyrin-Glycine Receptor Affinity by Multivalency*, in *ACS Chemical Biology*. 2014, American Chemical Society (ACS). p. 2554-2562.
49. Maric, H.M., et al., *Design and synthesis of high-affinity dimeric inhibitors targeting the interactions between gephyrin and inhibitory neurotransmitter receptors.* Angew Chem Int Ed Engl, 2015: p. 490-4.
50. Schulte, C., et al., *High-throughput determination of protein affinities using unmodified peptide libraries in nanomolar scale.* iScience, 2021.
51. Mäde, V., S. Els-Heindl, and A.G. Beck-Sickinger, *Automated solid-phase peptide synthesis to obtain therapeutic peptides*, in *Beilstein Journal of Organic Chemistry*. 2014, Beilstein Institut. p. 1197-1212.
52. Maric, H.M., et al., *Molecular basis of the alternative recruitment of GABA(A) versus glycine receptors through gephyrin.* Nat Commun, 2014. **5**: p. 5767.
53. Saiyed, T., et al., *Molecular Basis of Gephyrin Clustering at Inhibitory Synapses*, in *Journal of Biological Chemistry*. 2006, American Society for Biochemistry & Molecular Biology (ASBMB). p. 5625-5632.
54. van der Walt, S., et al., *scikit-image: image processing in Python*, in *PeerJ*. 2014, PeerJ. p. e453.
55. Hobro, A.J. and N.I. Smith, *An evaluation of fixation methods: Spatial and compositional cellular changes observed by Raman imaging*, in *Vibrational Spectroscopy*. 2017. p. 31-45.
56. O'Connell, M.A., B.A. Belanger, and P.D. Haaland, *Calibration and assay development using the four-parameter logistic model.* Chemometrics and Intelligent Laboratory Systems, 1993. **20**(2): p. 97-114.
57. Virtanen, P., et al., *SciPy 1.0: fundamental algorithms for scientific computing in Python.* Nature Methods, 2020. **17**(3): p. 261-272.
58. Lin, Y.-C., et al., *Genome dynamics of the human embryonic kidney 293 lineage in response to cell biology manipulations.* Nature Communications, 2014. **5**(1): p. 4767.
59. Hobro, A.J. and N.I. Smith, *An evaluation of fixation methods: Spatial and compositional cellular changes observed by Raman imaging.* Vibrational Spectroscopy, 2017: p. 31-45.
60. Tanaka, K.A.K., et al., *Membrane molecules mobile even after chemical fixation.* Nature Methods, 2010. **7**: p. 865-866.
61. Brock, R., I.H.L. Hamelers, and T.M. Jovin, *Comparison of fixation protocols for adherent cultured cells applied to a GFP fusion protein of the epidermal growth factor receptor.* Cytometry, 1999. **35**: p. 353-362.
62. Bogen, S.A., K. Vani, and S.R. Sompuram, *Molecular mechanisms of antigen retrieval: antigen retrieval reverses steric interference caused by formalin-induced cross-links.* Biotechnic & Histochemistry, 2009: p. 207-215.
63. Hoffman, E.A., et al., *Formaldehyde Crosslinking: A Tool for the Study of Chromatin Complexes.* Journal of Biological Chemistry, 2015. **290**: p. 26404-26411.
64. Richter, K.N., et al., *Glyoxal as an alternative fixative to formaldehyde in immunostaining and super-resolution microscopy.* EMBO J, 2018(1): p. 139-159.
65. Khayenko, V., et al., *A Versatile Synthetic Affinity Probe Reveals Inhibitory Synapse Ultrastructure and Brain Connectivity.* Angew Chem Int Ed Engl, 2022.

66. Schneider, A.F.L., et al., *Cellular uptake of large biomolecules enabled by cell-surface-reactive cell-penetrating peptide additives.* Nat Chem, 2021. **13**(6): p. 530-539.
67. Kasaragod, V.B., et al., *Elucidating the Molecular Basis for Inhibitory Neurotransmission Regulation by Artemisinins.* Neuron, 2019. **101**(4): p. 673-689.e11.
68. Kyte, J. and R.F. Doolittle, *A simple method for displaying the hydropathic character of a protein*, in *Journal of Molecular Biology*. 1982. p. 105-132.
69. Pedregosa, F., et al., *Scikit-learn: Machine Learning in Python.* Journal of Machine Learning Research, 2011. **12**(85): p. 2825-2830.

7 Acknowledgements

I want to express my gratitude towards Dr. Hans Michael Maric for giving me the opportunity to pursue my medical doctoral thesis in his lab. Thank you for the welcoming working environment and all the work and non-work-related discussions. Thank you Vladmir Khayenko for introducing me to all the relevant methods and technologies. I appreciated your mentorship and all the meaningful discussions we've had. Big thank you as well to Sonja Kachler for the great organisation of the lab and the technical support.

Thank you Clemens Schulte, not only for the MST measurements of the peptide probes but also for the conversations and feedback on presentation design. Thank you, Prof. Katrin Heinze, Mike Friedrich and Jürgen Pinnecker for your support in the field of confocal fluorescence microscopy. I would like to thank Prof. Carmen Villmann and Prof. Gernot Stuhler for being part of the thesis committee and giving much appreciated feedback throughout this project. I am grateful for the support from the Graduate School of Life Sciences of the Universtät Würzburg for supporting this thesis.

Finally, I would like to thank my family and friends for their love and support throughout all the years.

8 Supplementary

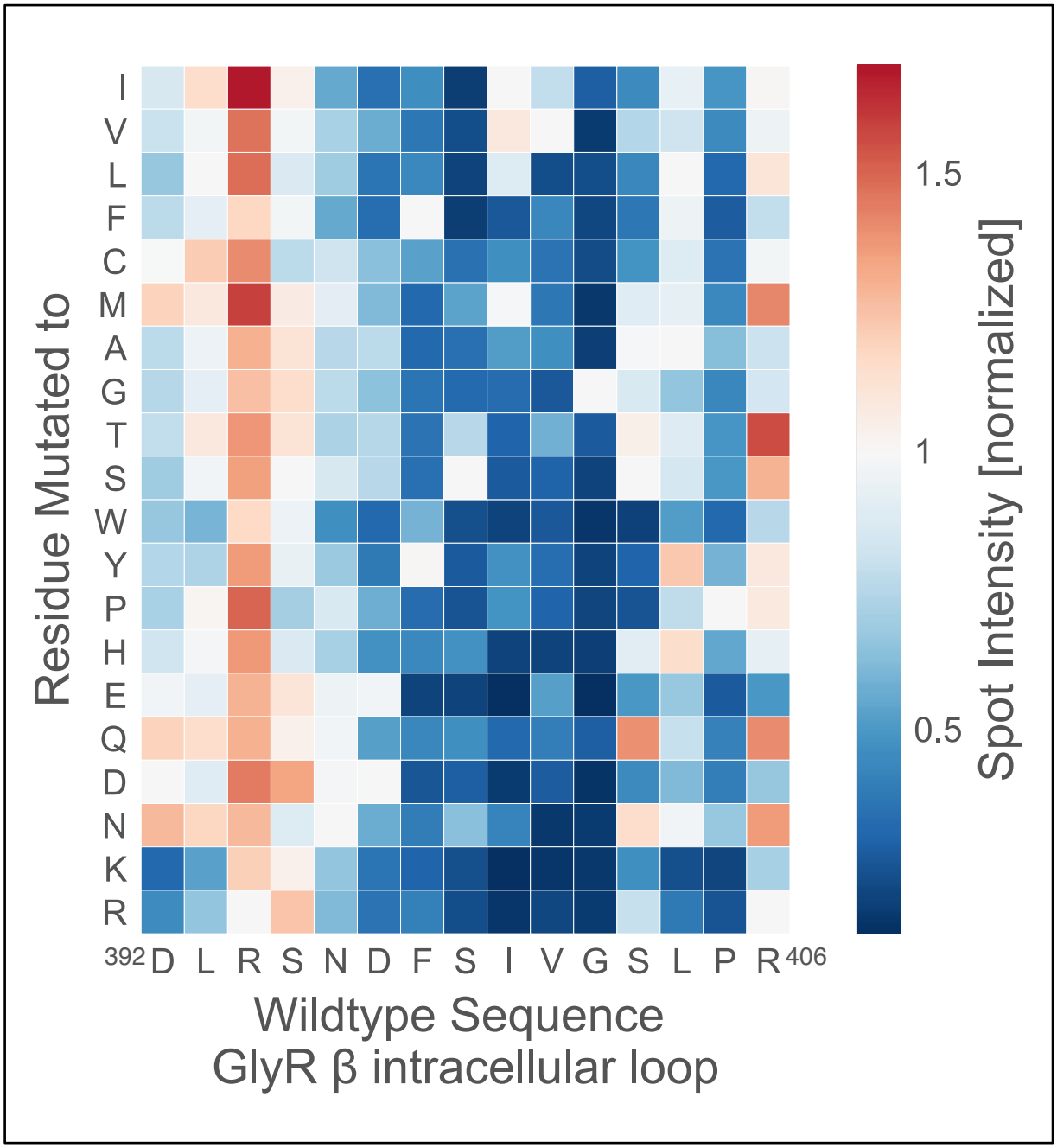

Supplementary Figure 1 Chemical space for amino acid mutations in the GlyR-core binding region for gephyrin is limited.Heatmap represents fold-change binding in gephyrin to GlyR-β peptide sequences. Native gephyrin contained in mouse brain lysate was used for peptide microarray binding. Intensities internally normalised to wild-type (WT)-peptide sequence. Blue indicates lower spot intensity; red indicates higher spot intensity compared to WT-residue. Residue mutated to ordered by Kyte & Doolittle hydrophobicity scale [68] where isoleucine is the most hydrophobic amino acid and arginine is the most hydrophilic amino acid. Data represented as mean of n=2. Data acquired by Clemens Schulte, RVZ Würzburg

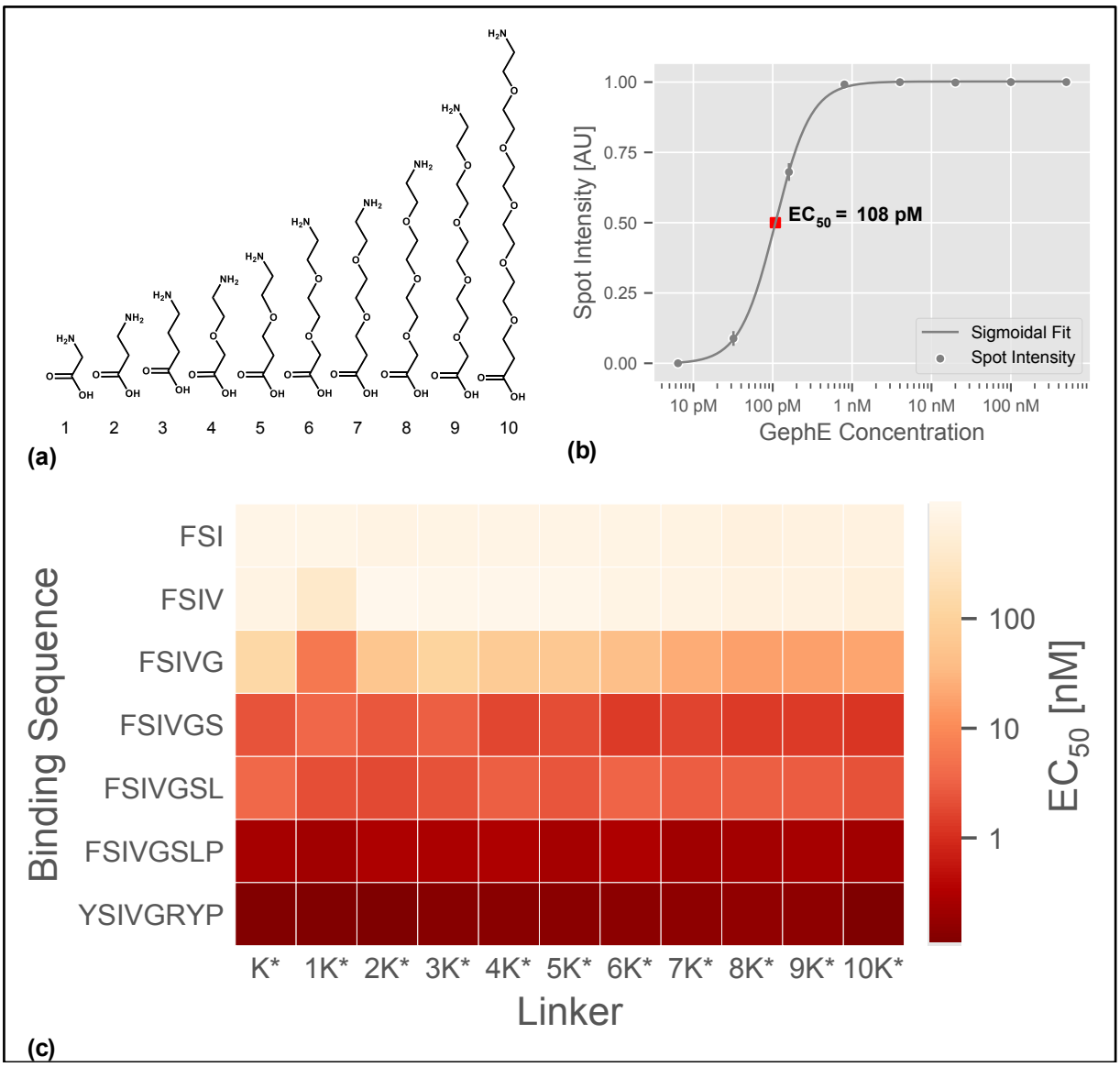

Supplementary Figure 2 Peptide binding sequence length has more influence on gephyrin binding as linker length. Linker region optimisation of peptide probe in microarray format. The modified amino acid K* (Fmoc-Lys(Fmoc)) was used for dimerization. **(a)** shows the different linkers used in this experiment (K*-10K*). **(b)** shows a sigmoidal fit for Epitope/Linker construct YSIVGRYP1K*. For fitting, four parameter logistic (4PL) regression was used as mentioned in Equation 8. Spot Intensity was measured for eight different gephE concentrations (n=2). **(c)** shows EC50 values as concentration of gephE for distinct dimeric gephE binding sequence/linker peptide constructs as a heatmap. EC_{50} specifies the calculated gephE concentration needed for half maximal intensity readout. Colour bar in logarithmic scale. Data represented as mean of n=2. Data acquired by Hans Michael Maric, RVZ Würzburg.

Supplementary Table 1 Detailed metrics for 4PL regression curve fitting (*see* Equation 8). Mean absolute error calculated using *scikit-learn* [69].

Probe	Region	c (EC_{50} [nM])	b	a	d	Mean absolute error
$_{C}$VK14	ROI_B	7.45	0.94	0.03	3.40	8.40
$_{C}$VK14	ROI_C	8764.83	1.43	1.42	174 939.94	7.90
$NN1D_C$	ROI_B	1.72	0.94	0.07	1.52	0.34
$NN1D_C$	ROI_C	2.27	21.86	0.26	1.43	0.31

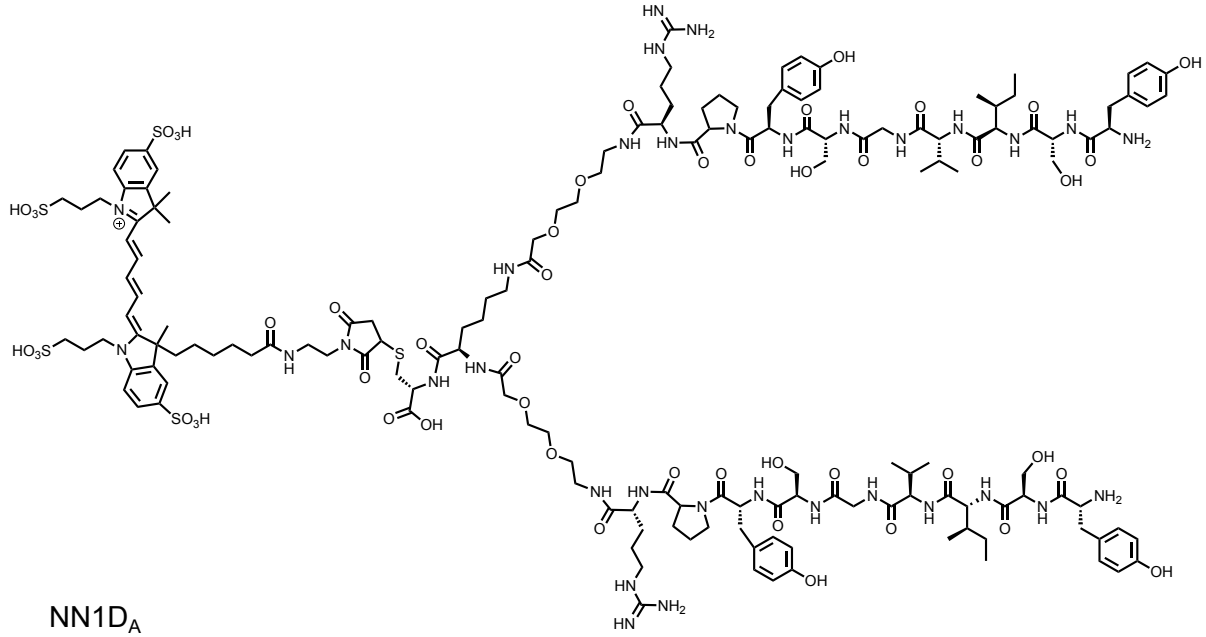

$NN1D_A$

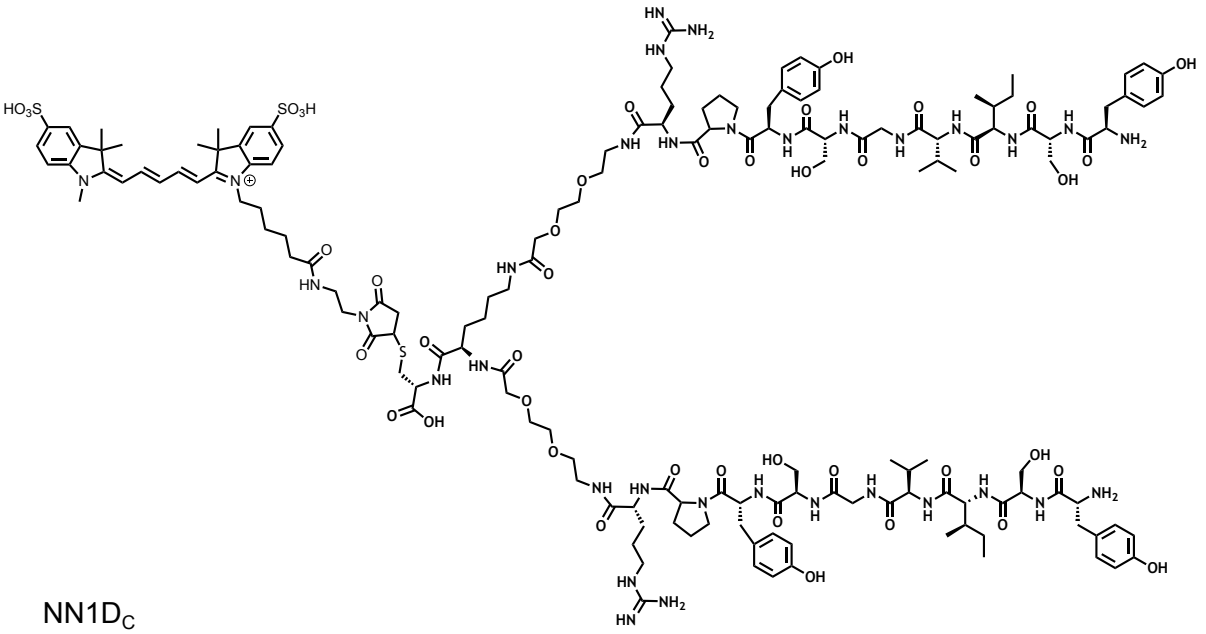

$NN1D_C$

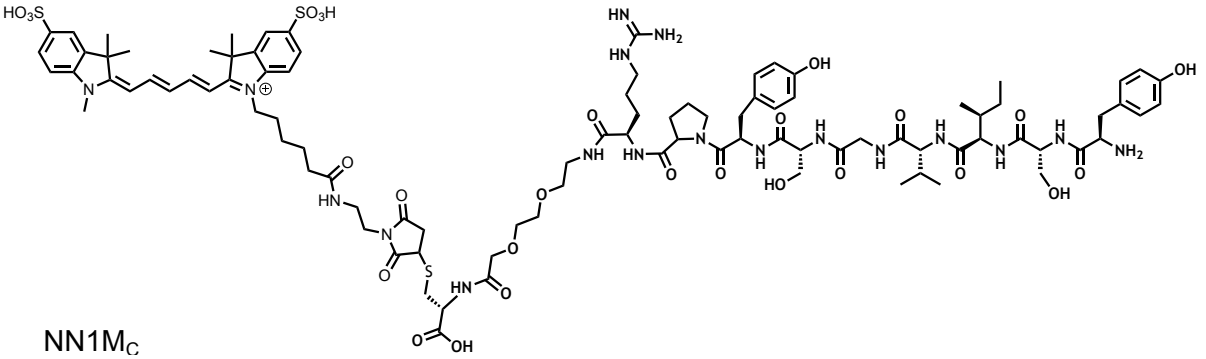

$NN1M_C$

Supplementary figure 3 Structural formulae of probes synthesised and tested.

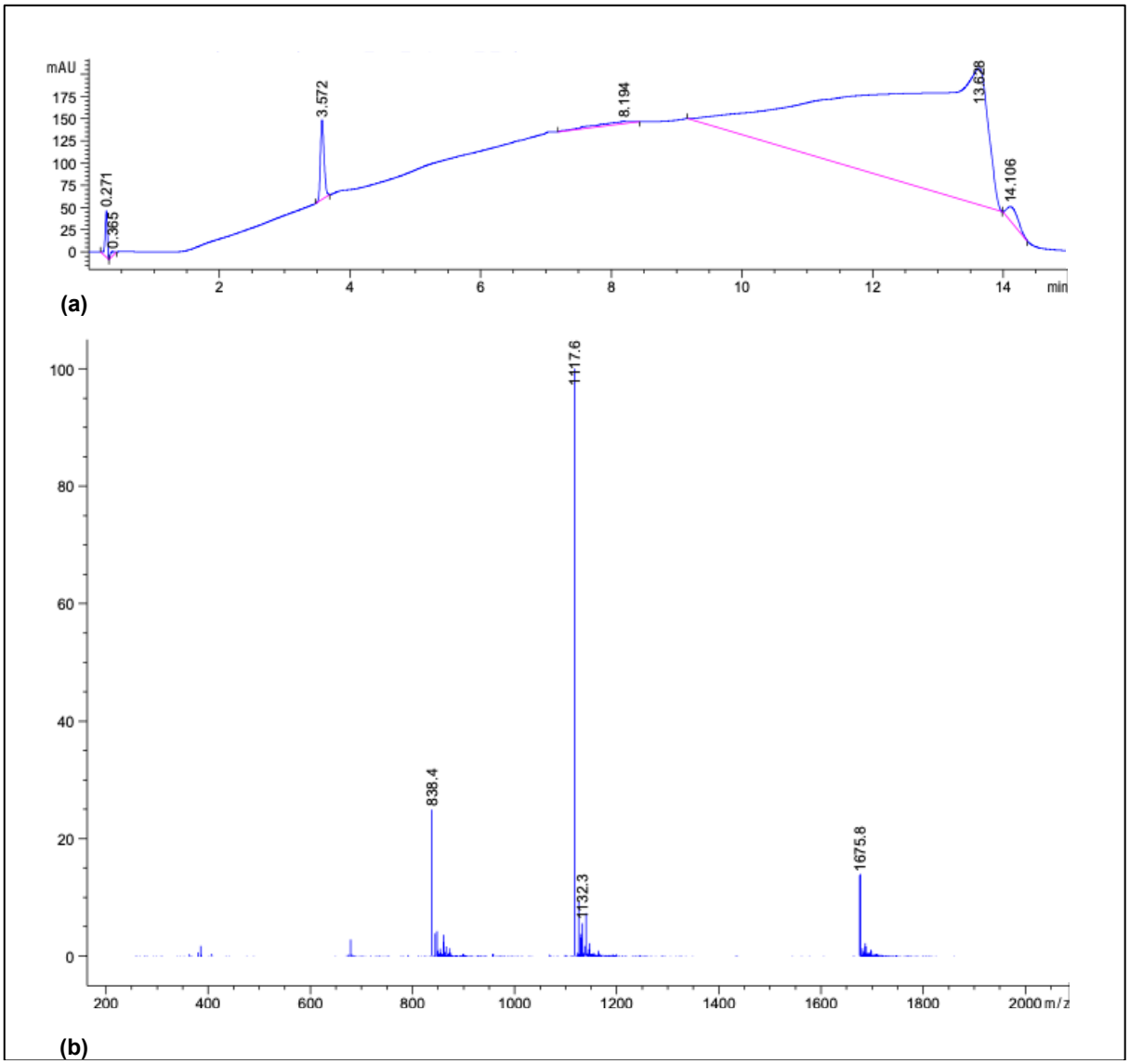

Supplementary figure 4 Confirmation of NN1D$_C$ synthesis. Purity exceeding 95% based on chromatogram **(a)**. UV-absorption at 215 nm was recorded with a main peak at 3.572 min (0-100% Buffer B in 10 min, Onyx™ Monolithic C18, LC Column 50 x 2 mm, *see* subsection 3.4). **(b)** shows mass spectrum (m/z) for main peak. Table to the right specifying ions observed, m/z observed, and m/z calculated.

Retention Time [min]	Ions obs	m/z obs	m/z calc
3.572	$[M+H]^{2+}$	1675.8	1675.9
	$[M+2H]^{3+}$	1117.6	1117.6
	$[M+3H]^{4+}$	838.4	848.4

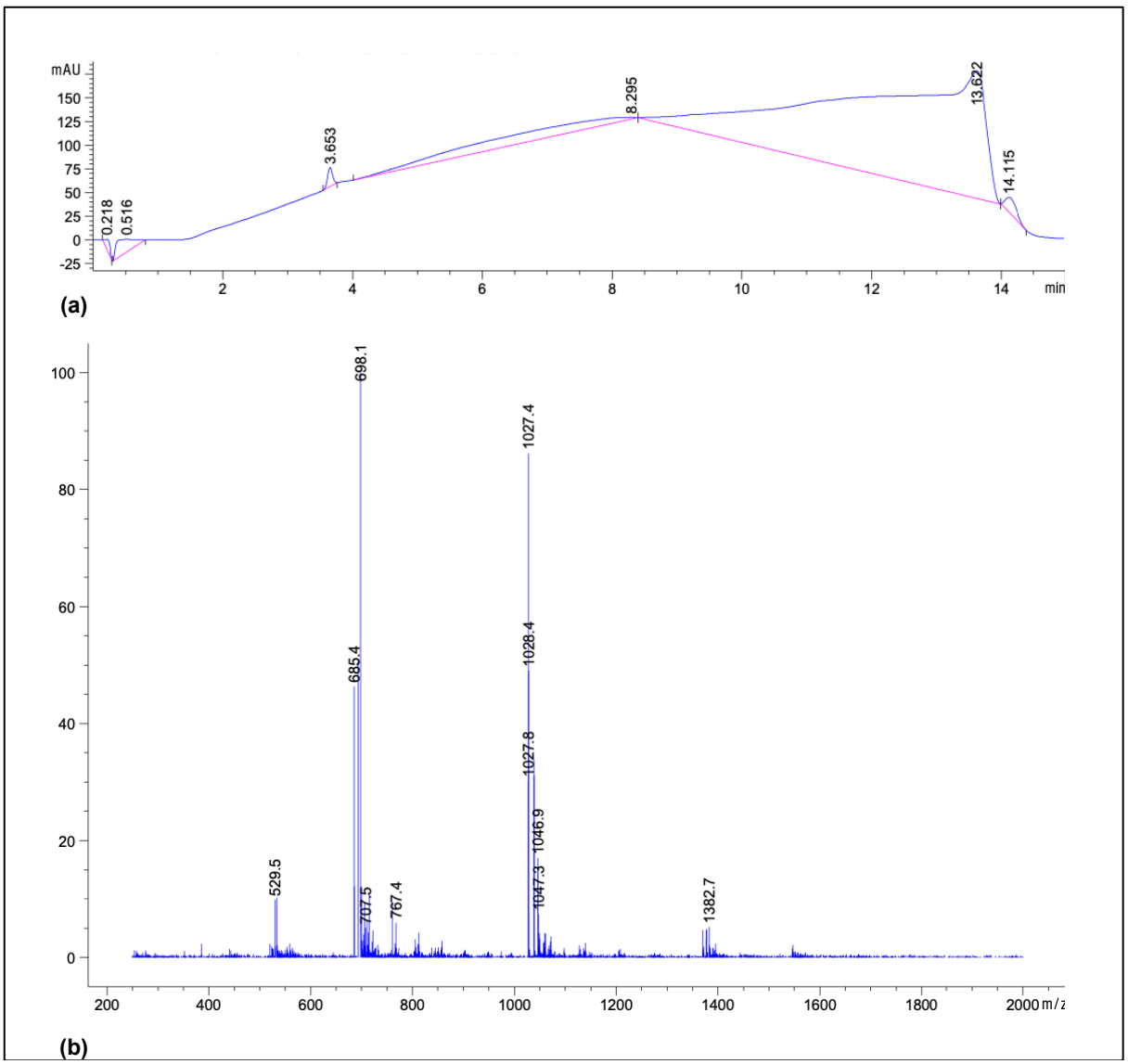

Supplementary Figure 5 Confirmation of $NN1M_C$ synthesis. Purity exceeding 95% based on chromatogram **(a)**. UV-absorption at 215 nm was recorded with a main peak at 3.653 min (0-100% Buffer B in 10 min, Onyx™ Monolithic C18, LC Column 50 x 2 mm, *see* subsection 3.4). **(b)** shows mass spectrum (m/z) for main peak. Table to the right specifying ions observed, m/z observed, and m/z calculated.

Retention Time [min]	Ions obs	m/z obs	m/z calc
3.653	$[M+H]^{2+}$	1027.4	1026.93
	$[M+2H]^{3+}$	685.4	684.96

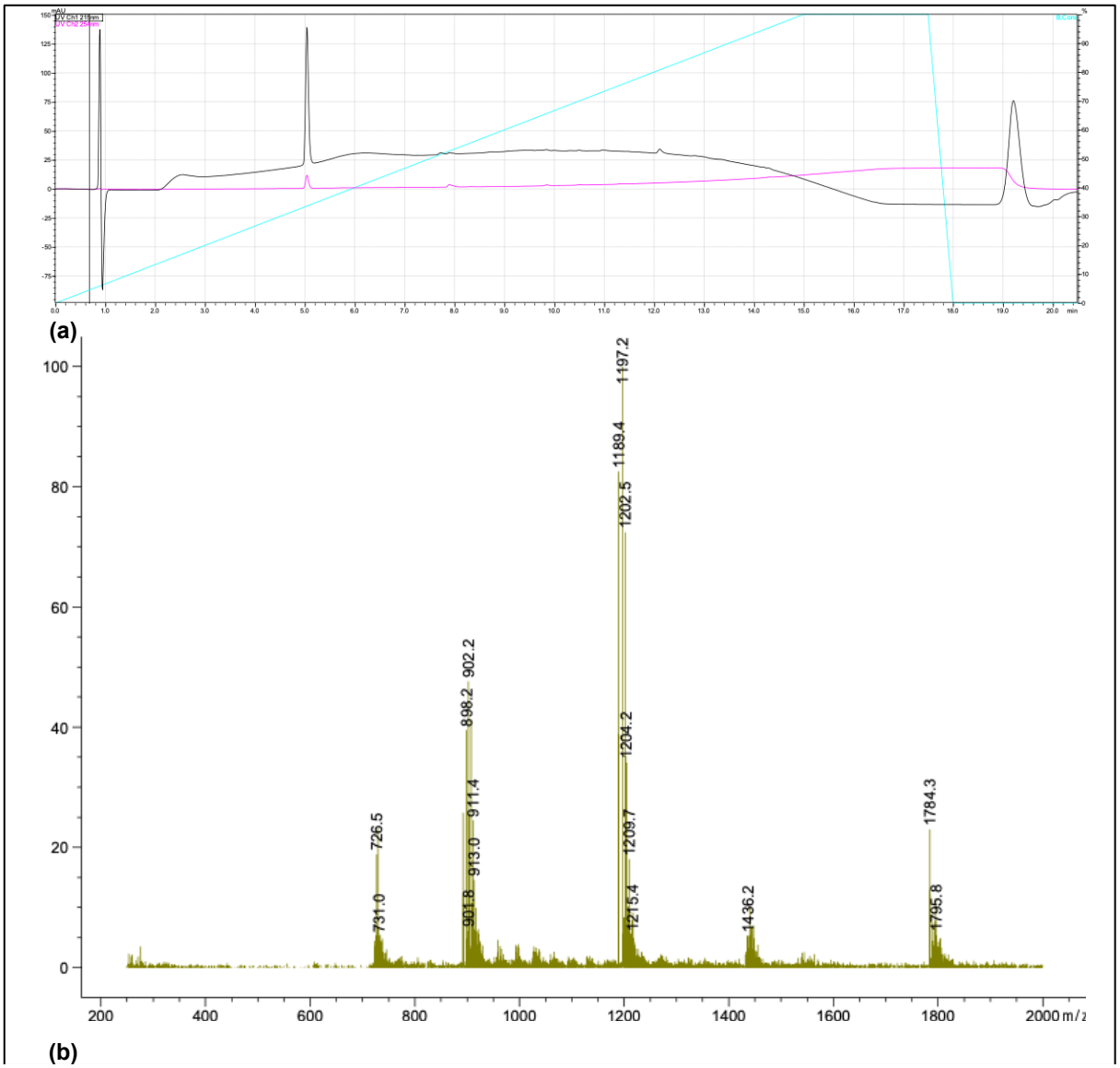

Supplementary figure 6 Confirmation of NN1D$_A$ synthesis. Purity exceeding 95% based on chromatogram **a)**. UV-absorption at 215 nm (black) and 254 nm (light magenta) was recorded with a main peak at 5 min (0-100% Buffer B in 15 min, Onyx^{TM} Monolithic C18, LC Column 100 x 4.6 mm, *see* subsection 3.4). **b)** shows mass spectrum (m/z) for main peak. Table to the right specifying ions observed, m/z observed, and m/z calculated at 5.1 min retention time.

Retention Time [min]	Ions obs	m/z obs	m/z calc
5.1	$[M+H]^{2+}$	1784.3	1784.3
	$[M+2H+Na]^{3+}$	1197.2	1197.2
	$[M+2H]^{3+}$	1189.4	1189.5
	$[M+2H+K]^{3+}$	1202.5	1202.2
	$[M+3H+K]^{4+}$	902.2	902.1
	$[M+3H+Na]^{4+}$	898.2	898.2
	$[M+4H+Na+K]^{5+}$	726.5	726.5

9 Figures

10 Tables

Curriculum vitae

The curriculum vitae is not available in the electronic version of this thesis.

Affidavit

I hereby confirm that my thesis entitled *Synthesis and Evaluation of Super Resolution Compatible Gephyrin Probes* is the result of my own work. I did not receive any help or support from commercial consultants. All sources and / or materials applied are listed and specified in the thesis.

Furthermore, I confirm that this thesis has not yet been submitted as part of an other examination process neither in identical nor in similar form.

Berlin, 22.09.2022

Eidesstattliche Erklärung

Hiermit erkläre ich an Eides statt, die Dissertation *Synthese und Evaluation von Gephyrinsonden für hochauflösende Mikroskopieverfahren* eigenständig, d. h. insbesondere selbständig und ohne Hilfe eines kommerziellen Promotionsberaters, angefertigt und keine anderen als die von mir angegebenen Quellen und Hilfsmittel verwendet zu haben.

Ich erkläre außerdem, dass die Dissertation weder in gleicher noch in ähnlicher Form bereits in einem anderen Prüfungsverfahren vorgelegen hat.

Berlin, 22.09.2022